A MODEL OF MAGNETIC HYPERTHERMIA

FLEUR BURROWS

Submitted for the Degree of Master of Science

THE UNIVERSITY OF YORK

DEPARTMENT OF PHYSICS

MARCH 2012

List of Corrections

Page 3: Line 3, typo fixed.

Page 13: Figure 3, expanded caption.

Page 13-19: Figures 2-7, added references.

Page 15: Line 6, typo fixed.

Page 16: Lines 6 and 10, typos fixed.

Page 20: Figure 8, typo on axis label fixed.

Page 28: Figure 14, expanded caption, added paragraph relating to parameters in clinical trials.

Page 29: Figure 15, axis label added.

Page 31: Lines 6, 16 and 24, typos fixed.

Page 33: Line 19, typo fixed.

Page 37: Section 3.5, Objectives added.

Page 38: Second paragraph, reference added.

Page 40: Line 4, typo fixed.

Page 41: Section 4.5 line 5, typo fixed.

Page 42: Line 5, typo fixed.

Page 44: Line 4th from bottom, typo fixed.

Page 48: Equation 61, H_k changed to H_K

Page 49: 2nd paragraph, uniaxial anisotropy for iron nanoparticles justified, reference added.

Page 57: Line 3rd from bottom, typo fixed.

Page 58: Figure 34, typo in y-axis label fixed.

Page 61: Appendix, added title.

Page 70: Third symbol, clarified definition.

Page 73: Reference 18, typo fixed.

Page 74: Reference 35, typo fixed.

Page 75: Reference 44, 45 and 53, typos fixed.

Abstract

A magnetic material exposed to a field that is cycled is observed to become warm. This arises because any misalignment between the field and the moment causes the generation of magnetostatic energy dissipated as heat. This effect is known as magnetic hyperthermia, and can be used as a medical therapy where fine particles are used as the magnetic medium. In a practical application where low fields ($H < 250\,Oe$) are used, the mechanism of heating is not well understood and can be due to losses in a hysteresis cycle, susceptibility loss, or frictional heating due to particle rotation in a liquid environment. In this work a theoretical study has been undertaken of hysteresis loss using Monte-Carlo techniques. It has been found that there is a maximum in the power loss and therefore heat generated with frequency occurring in the range 1 to $10\,kHz$ which depends only weakly on particle size. However, for small particles ($D_m < 10\,nm$) the frequency of the peak depends strongly on packing fraction due to the effects of dipolar interactions. The hysteresis loss reduces significantly when a non-saturating field is used especially for high packing fractions where the field produced by dipolar interactions is stronger, which causes micromagnetic configurations to form that favour the demagnetised state.

Contents

List of Figures

Acknowledgements

I would like to thank my supervisors, for their encouragement and support during my years at York; Kevin O'Grady, Roy Chantrell and Yvette Hancock.

Thanks are also due to the people in the magnetism groups who have contributed to this project, and who have given me guidance and advice over the past two years.

Declaration

I declare that the work presented in this thesis is based purely on by own research, unless otherwise stated, and has not been submitted for a degree in either this or any other university.

Signed

Fleur Burrows

1 INTRODUCTION

When a magnetic moment is exposed to a field with which it is not aligned there exists a magnetostatic energy. The moment will reduce its magnetostatic energy by rotating to align with the field. Therefore an energy loss results in a process called magnetic hysteresis. If a low field strength is applied at a high frequency this generally results in the inability of the moment to follow the field. This phase lag also generates heat independent of the moment alignment process. Hence a physical rotation of the material containing the magnetic moment also causes heating along with frictional effects. These magnetic heating effects are known collectively as magnetic hyperthermia.

1.1 Hyperthermia Therapy

Hyperthermia therapy is the process of treating cancer with the application of heat. Usually this is used in conjunction with other methods of treatment, and involves raising the temperature of the cells to between $40 - 43°C$ [1]. As an isolated therapy, if the temperature is increased above $43°C$ and maintained for between 30–60 minutes the heated cells burst in a process known as necrosis, causing shrinkage in tumour size [2].

The efficiency of this method, common to all forms of hyperthermia therapy, is not good enough when applied alone to replace the more conventional treatments of radiotherapy and chemotherapy for most cancers [3]. However, for certain types of cancer these methods are very difficult to use or do not work effectively because the tumour is located close to vital organs or is drug resistant. In these cases hyperthermia is a viable alternative.

As an adjunct therapy 'mild temperature hyperthermia', below $43°C$ does not directly cause cell death but can increase the effectiveness of the standard treatments. For example, certain chemotherapy drugs are more active at higher temperatures resulting in a requirement for a lower dose and decreasing the damage they cause elsewhere in the body This is advantageous for reducing the side effects of the drugs.

The mechanism by which chemotherapy drugs kill cells is different for each type of drug and consequently hyperthermia can interact with the process in a different ways. For some commonly used chemotherapy drugs heating has no effect on toxicity and in others it can increase drug tolerance of the cells [4]. Therefore the types of drug suitable for combined treatment and the temperatures required need to be investigated on a case by case basis.

Radiotherapy has also shown good synergy with hyperthermia [5], provided the treatment is managed properly. In solid tumours the uncontrolled growth of the cancerous cells results in a poor

vascular structure and consequently low pH and oxygen concentrations. Cells in these conditions are particularly resistant to radiation damage due to the low quantity of free radicals that can be ionised. Heating of the tumour dilates the blood vessels increasing blood flow, and thereby increasing the availability of oxygen in the region [6]. As an added effect the poor vascular structure makes it more difficult for the tumour to dissipate excess heat in comparison to the surrounding healthy tissues [7].

1.2 Methods of Heating

Hyperthermia can be used on a range of scales, suited to different situations. Metastatic cancer is the term for when some cancerous cells have broken away from their original location and seeded multiple tumours throughout the body, often by entering the circulatory system. This requires whole body hyperthermia initiated using thermal chambers or hot water blankets to increase core body temperature while chemotherapy drugs are administered, in combination this treatment is known as thermochemotherapy. The highest temperature it is safe to use is $42°C$, set by liver which is the least thermotolerant normal tissue [8].

Whole body hyperthermia often causes unpleasant side effects such as nausea, dizziness, and vomiting. Consequently it is not desirable to heat the entire patient unnecessarily and so for cancers localised in limbs or organs only the immediate region is treated. In some cases, such as abdominal cancers the patients blood is removed, heated and reintroduced into the body along with heated drugs. Other methods rely on microwave or radiofrequency electromagnetic radiation focused on the area, but all of the above methods are impossible to target well enough to avoid heating healthy cells as well as those which are malignant.

Finally, local hyperthermia is well suited to treating small, solid, well-defined tumours. For this microwave, radiofrequency and ultrasound are also used to generate heat, but the heating is targeted directly at the tumour site through an array of probes inserted throughout the tumour volume. This is preferable where possible as it heats the healthy tissues to a minimal degree. The array must be very uniformly arranged as variations in spacing results in cool spots which severely reduce the effectiveness of the treatment. As an alternative to probes, millimetre scale particles of ferromagnetic alloys known as thermoseeds have been arranged inside tumours and exposed to high frequency magnetic fields [9]. As the magnetic moments of the particles move within the alternating field heat is produced.

1.3 Magnetic Hyperthermia

A relatively recent innovation was the use of magnetic nanoparticles in the form of a ferrofluid, this method is termed 'magnetic fluid hyperthermia'. Here nanoparticles can be injected either directly into the tumour or intravenously in a colloidal suspension [10]. This method can be used to target the cancerous cells specifically rather than the general area of the tumour in a manner that is less invasive than interstitial arrays or thermoseeds. Once the magnetic nanoparticles are in place they are subjected to a high frequency alternating magnetic field, similarly to the thermoseeds. However, nanoparticles can produce significantly larger amounts of heating than the larger particles. This is because there are a number of independent heating mechanisms which can happen simultaneously, some of which are significantly stronger for particles in a low size range.

Aside from the benefit of convenience to the patient there are other reasons why nanoparticles are a better method of providing the heat generation. Uniformity of particle distribution should be easier to achieve with a greater number of smaller particles which will ensure uniform heating, especially in irregularly shaped tumours. Nanoparticles have demonstrated good stability in vivo when an appropriate coating is used [11], which can allow the applications of multiple heat treatments over several weeks following one injection [12].

Nanoparticles are also small enough to be absorbed into cells which are typically $10 - 100\,\mu m$ in diameter through the cell wall [13]. It has been reported that magnetic nanoparticles could be bound to molecules or proteins which are only taken up by the cancerous cells, in a similar fashion to how radioactive tags are used in medical imaging [14]. This method could apply maximum heat to the malignant cells and could also release cell-killing drugs within them without damaging the surrounding tissues.

2 THEORY

2.1 Hysteresis in Ferromagnets

Ferromagnets are metals in which it is energetically favourable for the magnetic moments due to unpaired electron spins on neighbouring atoms to align parallel. As a result of this spontaneous alignment a ferromagnet can maintain a net magnetisation in zero field, it can also be fully magnetised by a relatively weak external field. The value of the saturation magnetisation, when every moment in the ferromagnet aligns is a intrinsic property of each material, denoted by M_s. The net magnetisation retained in the absence of an applied field is called the remanence, M_r.

Magnetic hysteresis refers to how a ferromagnet can be in multiple magnetic states whilst subject to the same external conditions, depending on the previous magnetisation of the material. For example two identical ferromagnets having been subject to a positive and negative saturating field respectively, will have equal but opposite remanent magnetisations when the field is removed. It is not possible to know the magnetisation of the material from only its present environment, its previous state must also be known.

As ferromagnets can remain magnetised in the absence of a magnetic field an input of energy is required to reduce the material to a demagnetised state. This can either be in the form of heating; above a critical temperature unique to each material (the Curie point, T_C) all ferromagnets lose their magnetic properties. Or, an increasing negative applied field will reduce the magnetisation as the reverse direction of magnetisation becomes more energetically favourable. The point at which the magnetisation passes through zero is called the coercivity or coercive field, H_c.

When subject to an external magnetic field, the magnetisation of a ferromagnet plotted against the applied field traces out a loop characterised by the coercivity and remanence of the material, as shown in figure 1. Energy input is required to rotate a magnetic moment from one energy minimum to another through an energetically unfavourable orientation, and this energy is released as heat when the moment returns to a low energy state. The area of a hysteresis curve is proportional to the energy released as heat in one complete cycle of the applied field as described in equation 1.

$$E_H = M_s \int M dH \tag{1}$$

The energy lost as heat because of the area of the loop is called the hysteresis loss. The rotation of moments through an energy barrier to lie in minima closer to the direction of an applied field produces the irreversibility that results in hysteresis losses.

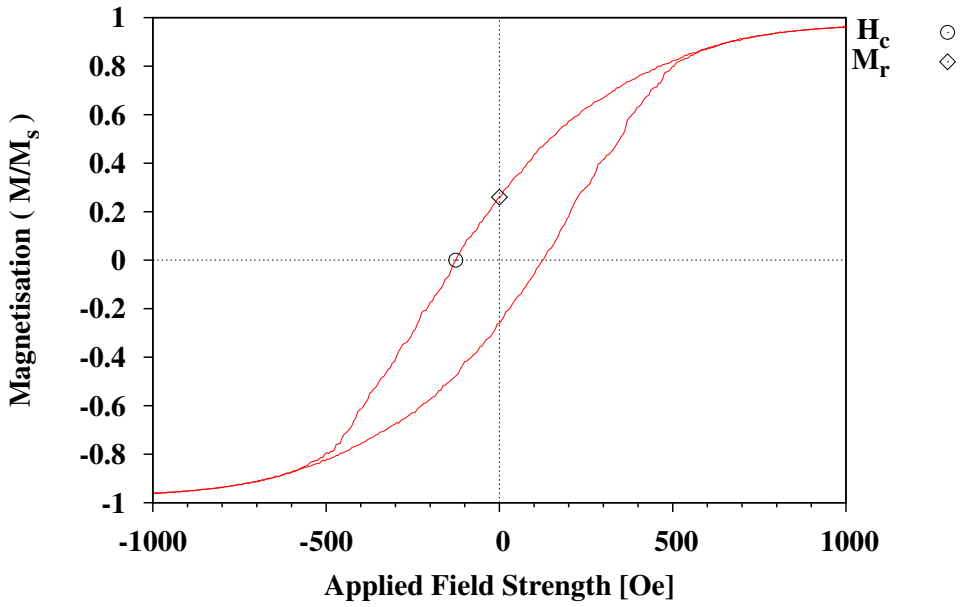

Figure 1: Simulation of a hysteresis loop for an iron composite at 0.05 packing fraction with particle diameters of $20\,nm$ and a frequency of $1\,kHz$. Coercivity and Remanence are marked.

2.2 Domain Processes and Hysteresis

The spontaneous magnetisation of ferromagnets is caused by a short range effect called the exchange interaction, arising from the quantum mechanical nature of electrons. Over long ranges this effect is dominated by the dipole-dipole interaction and the demagnetising field; both work to reduce the net magnetisation. Consequently within ferromagnets a domain structure forms, see figure 2, which works to minimise the energy of the two competing effects. Within domains there is a uniform magnetisation M_s, and the direction of magnetisation does not align with that of neighbouring domains. Domains are typically 10^{-2} to $10\,\mu m$ across, encompassing 10^{12} to 10^{18} atoms.

Domains are separated by domain walls with widths of approximately 100 atoms. At these points the directions of the individual moments incrementally rotate from that in one domain the next. When a field is applied the walls shift; expanding the domains already strongly magnetised in the same direction as the field at the expense of the less energetically favourable domains surrounding them, shown in figure 3. This mechanism is that which allows a relatively weak applied field to strongly magnetise a ferromagnet.

The direction of magnetisation within a domain is likely to have a preferred orientation or easy axis, this is called the anisotropy. Dislocations in crystallographic structure or impurities in the

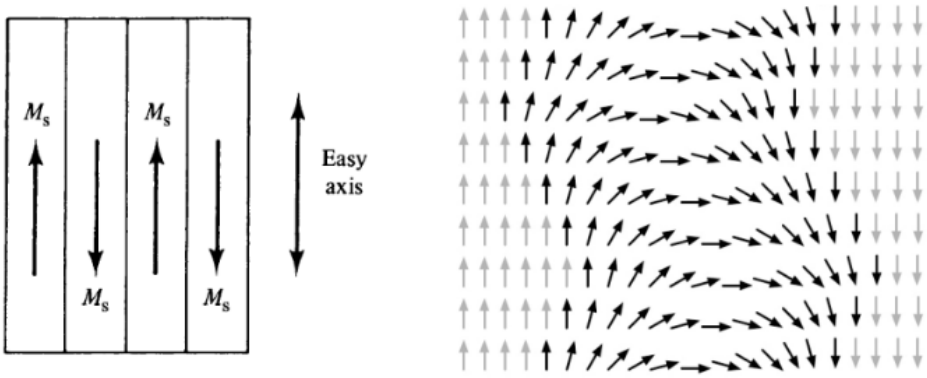

Figure 2: Domain structure in a crystal with uniaxial anisotropy (one easy axis). Close up representation of individual moments in a 2-D domain wall of finite width [15].

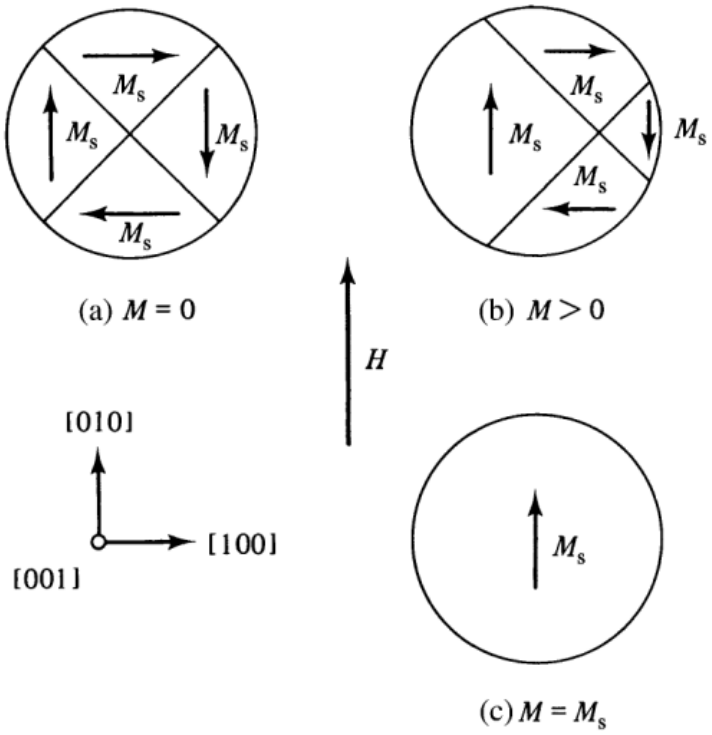

Figure 3: Domain wall motion enlarges favourable domains under the influence of an increasing external field: (a) before field is applied, (b) as field strength increases, (c) material is saturated [15].

material can produce sticking points in the otherwise smooth motion of domain walls. The change in anisotropy strength or direction at these points increase the energy barrier to rotating the moments in the domain wall, requiring a stronger applied field. This phenomenon is referred to as domain wall pinning, a useful tool for decreasing the probability of a ferromagnet reverting to a demagnetised state without a significant input of energy.

There are multiple factors which contribute to the anisotropy, however some have only very small effects and the total anisotropy can be approximated by the dominant term. Magnetocrystalline,

or simply crystal anisotropy arises due to the spin-orbit interaction, generally a relatively weak coupling as it can be overcome by application of an applied field of a few hundred oersteds. The direction of the easy axis and the magnitude of anisotropy in bulk material is dependent on the crystal structure.

Uniaxial anisotropy is when there is only one easy axis, this occurs in hexagonal or tetragonal crystals where anisotropy strength is symmetrical around the c-axis. Consequently the energy of the anisotropy can be expressed as a series of expansions of cosines of the angle θ between the direction of the saturation magnetisation relative to the crystal axes. The form of the equation is normally converted to use sines, as in equation 2. The important information for reversal is the change in energy with angle and as K_0 is not dependent on the angle it can be neglected. When K_1 and K_2 are both positive the energy minimum is located at $\theta = 0$, so the easy axis lies along the c-axis. The K_2 term, as it is multiplied by the fourth power of $sin(\theta)$, is often so small that it can also be neglected.

$$E_{\text{uniaxial}} = K_0 + K_1 sin^2(\theta) + K_2 sin^4(\theta) + ... \tag{2}$$

$$E_{\text{cubic}} = K_0 + K_1(\alpha_1^2\alpha_2^2 + \alpha_2^2\alpha_3^2 + \alpha_3^2\alpha_1^2) + K_2(\alpha_1^2\alpha_2^2\alpha_3^2) + ... \tag{3}$$

Cubic anisotropic materials usually have easy axes along the [100] and other symmetric directions. The anisotropy energy has a similar form to that for hexagonal crystals. In equation 3 for neatness; α_1, α_2, and α_3 are the cosines of the three angles that the direction of magnetisation makes with the crystal axes a, b, and c.

2.3 Single Domain Particles

Domain walls have an energy associated with them which is proportional to their cross-sectional area, and the magnetostatic energy of a domain is proportional to its volume. At some point a particle can be so small that its energy when fully magnetised is lower than the energy it would have with two domains. These are called single domain particles. The critical size for the upper limit of a single domain particle in a system of adjacent interacting particles is shown in equation 4 Here μ is the value of a single magnetic moment and γ is the energy density of the domain wall [16].

$$r_c = \frac{0.135\mu\gamma}{M_s^2} \tag{4}$$

The size range over which particles are considered single domain is small. Above diameters of a few tens of nanometres most ferromagnets break into multiple domains, and when particles become sufficiently small they become superparamagnetic. Superparamagnetism is when the magnetisation

of a particle reverses continually due to thermal energy fluctuations, and is explained in more detail in section 2.6.

Although particles are always considered to be perfect spheres, in reality even the most carefully manufactured specimen will have some deformation. The deformations on particles only hundreds of atoms across are tiny, but they mean the particle is properly considered elliptical (or a prolate spheroid). The demagnetising field in the particle, caused by the net magnetisation is therefore lower the moment is parallel to the longest axis. This leads to the anisotropy due to shape favouring an orientation of the particle along its longest length, a uniaxial anisotropy. Equation 5 gives the expression for shape anisotropy, where N_c and N_a are demagnetising factors along the long and short axes of a particle respectively.

$$K_s = \frac{1}{2} M_s^2 (N_c - N_a) \tag{5}$$

Crystal and shape anisotropy will usually favour different directions of magnetisation, and which type dominates depends on the degree of deviation from spherical of the single domain particle. A major/minor axis ratio of $c/a > 1.1$ is large enough to produce dominant shape anisotropy, this is because K_s is proportional to the square of M_s. Consequently only in a few materials with extremely high crystal anisotropies such as BaFe and FePt, does crystal anisotropy need to be taken into account for single domain nanoparticles. In general, crystal anisotropy is the strongest contributor to the anisotropy field in bulk materials, however in most single domain particles it is a negligible term compared to the uniaxial anisotropy caused by the particle shape.

2.4 Stoner-Wohlfarth Theory

The energy barrier between easy axes in a ferromagnetic particle is described by The Stoner-Wohlfarth Model [17]. This assumes an isolated single domain particle. The particle is considered to be a prolate spheroid in which the anisotropy is due to the shape and is uniaxial. The mechanism of reversal is coherent rotation of the magnetisation. There are other mechanisms for reversal, however the model used in this work does not apply incoherent rotation mechanisms and so they are not discussed here.

First, for the case when moment and easy axis are aligned parallel with the field antiparallel, the energy barrier to reversal is simply the anisotropy energy $\Delta E = KV$. To reverse the moment the applied field energy must exceed ΔE. When it does the moment suddenly flips from a positive to negative direction. This is the anisotropy field H_K, as it is the field strength which overcomes the anisotropy energy.

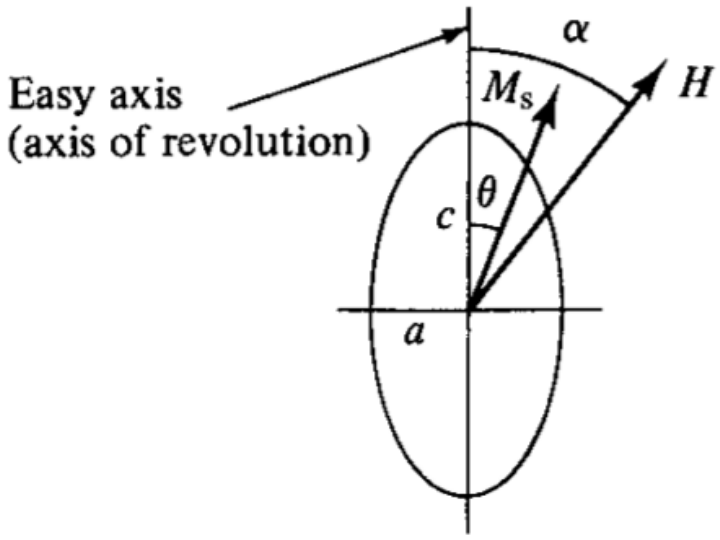

Figure 4: A single domain magnetic particle with an external magnetic field applied at an angle α and the particle's magnetic moment at an angle θ to the easy axis [15].

When the field lies at an angle α to the easy axis, the moment rotates out of the easy axis by an angle θ due to the torque on the moment, as shown in figure 4. The energy of the particle is then calculated from the anisotropy energy minus the Zeeman energy (eqn. 6). The energy density in J/m^3 can be minimised (eqn. 7).

$$E = KVsin^2(\theta) - \mu_0 M_s V H cos(\alpha - \theta) \tag{6}$$

$$\frac{dE}{d\theta} = 2Ksin(\theta)cos(\theta) + \mu_0 M_s H sin(\alpha - \theta) = 0 \tag{7}$$

When the field is perpendicular to the easy axis ($\alpha = 90°$; $sin(\alpha) = 1$):

$$2Ksin(\theta)cos(\theta) = \mu_0 H M_s cos(\theta) \tag{8}$$

From equation 8, the anisotropy field H_K can be found as it is the value of H when $\theta = 90°$:

$$H_K = \frac{2Ksin(\theta)}{\mu_0 M_s} = \frac{2K}{\mu_0 M_s} \tag{9}$$

Starting with equation 6 again, the energy barrier to reversal for the particle can be found. The applied field H is considered to be initially aligned with the easy axis in the opposite direction to the moment of the particle. The minimum energy for the moment is therefore at the point where $\theta = 180°$, which is shown in equation 12 .

$$\frac{\mathrm{d}E}{\mathrm{d}\theta} = 2KVsin(\theta)cos(\theta) + \mu_0 M_s V H sin(\theta) = 0 \tag{10}$$

$$0 = sin(\theta)(2KVcos(\theta) + \mu_0 M_s V H) \tag{11}$$

$$E_{\text{min}} = \mu_0 M_s V H \tag{12}$$

If the angle at which E is at maximum is unknown, finding $cos(\theta)$ from equation 11 and substituting into equation 6 produces an angle independent formula for E_{max} (eqn. 17).

$$cos(\theta) = -\frac{\mu_0 M_s V H}{2KV} = -\frac{\mu_0 M_s H}{2K} \tag{13}$$

$$E_{\text{max}} = KV(1 - cos^2(\theta)) - \mu_0 M_s V H cos(\theta) \tag{14}$$

$$E_{\text{max}} = KV\left(1 - \frac{\mu_0^2 M_s^2 H^2}{4K^2}\right) + \frac{\mu_0^2 M_s^2 V H^2}{2K} \tag{15}$$

$$E_{\text{max}} = KV\left(1 - \frac{\mu_0^2 M_s^2 H^2}{4K^2} + \frac{\mu_0^2 M_s^2 H^2}{2K^2}\right) \tag{16}$$

$$E_{\text{max}} = KV\left(1 + \frac{\mu_0^2 M_s^2 H^2}{4K^2}\right) \tag{17}$$

The energy barrier $\Delta E = E_{\text{max}} - E_{\text{min}}$ is found by from equations 12 and 17 and is simplified using the substitution of H_K as defined in equation 9. This gives ΔE purely as a function of material constants, applied field strength, and the volume of the particle (eqn. 19).

$$\Delta E = KV\left(1 + \frac{\mu_0^2 M_s^2 H^2}{4K^2}\right) - \mu_0 M_s V H = KV\left(1 + \frac{\mu_0^2 M_s^2 H^2}{4K^2} - \frac{\mu_0 M_s H}{K}\right) \tag{18}$$

$$\Delta E = KV\left(1 - \frac{H}{H_K}\right)^2 \tag{19}$$

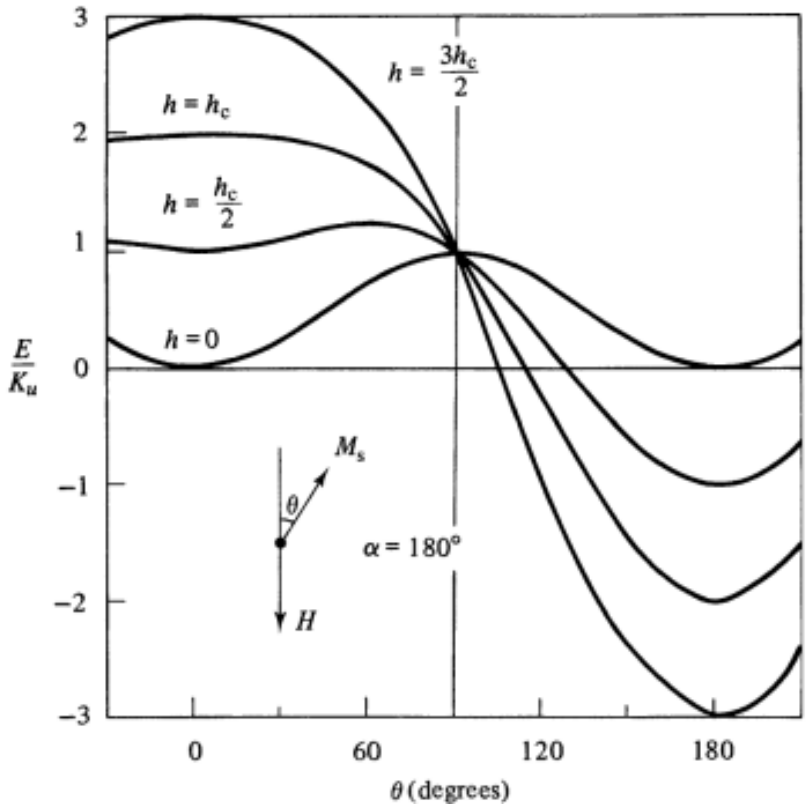

Figure 5: The shape of the energy barrier to magnetic reversal inside a particle depends on the strength of the external field and the angle θ at which it is applied [15].

The shape of the normalised energy barrier in a single particle for varying field strengths is shown in figure 5. It is calculated from the total energy E as a function of θ when α is constant at $180°$. The Stoner-Wohlfarth equation used to plot these curves is a modified form of equation 6 and is given below (eqn. 20). Here K_u is the uniaxial anisotropy constant and the volume V has been set equal to 1; making $h = H/H_K$ a reduced field and E/K_u a reduced energy.

$$\frac{E}{K_u} = sin^2(\theta) - h\,cos(\alpha - \theta) \tag{20}$$

Figure 6 shows the hysteresis loop dependence on the angle α between H and the easy axis for a system of non-interacting single domain particles with uniaxial anisotropy. Here h is again a reduced field and $m = M/M_s$ is the normalised magnetisation. The coercivity is very sensitive to the angle of the applied field. $H_c = H_K$ when $\alpha = 0$, but if the alignment is off by only 10% it leads to a 30% reduction in the value of H_c

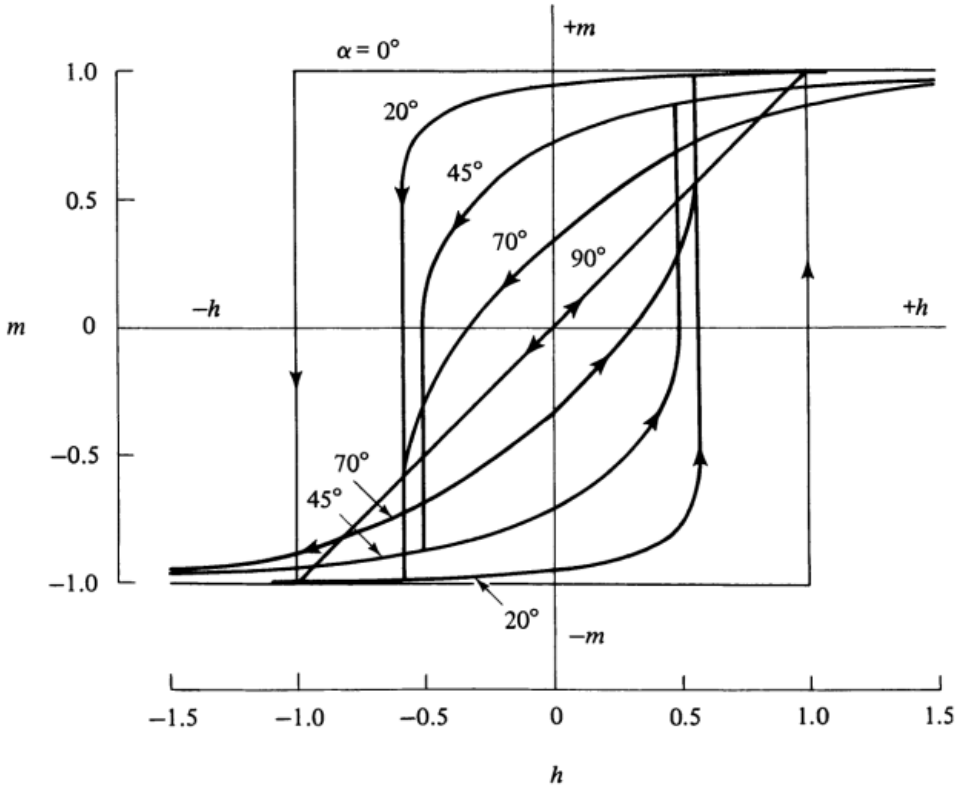

Figure 6: Hysteresis loops for single domain particles with uniaxial anisotropy for a range of angles between the field and easy axis [15].

The Stoner-Wohlfarth model can be extended to consider a system of particles in which the direction of anisotropies is distributed randomly in 3-D space. This can produce an overall magnetically isotropic system, which is a more realistic case. The remanence is then reduced to $0.5M_s$ and the coercivity is $0.48H_K$, this value is calculated from the random average in 3-D of $cos(\theta)$. An example hysteresis loop using a reduced field h and normalised magnetisation m for such a system is shown in figure 7.

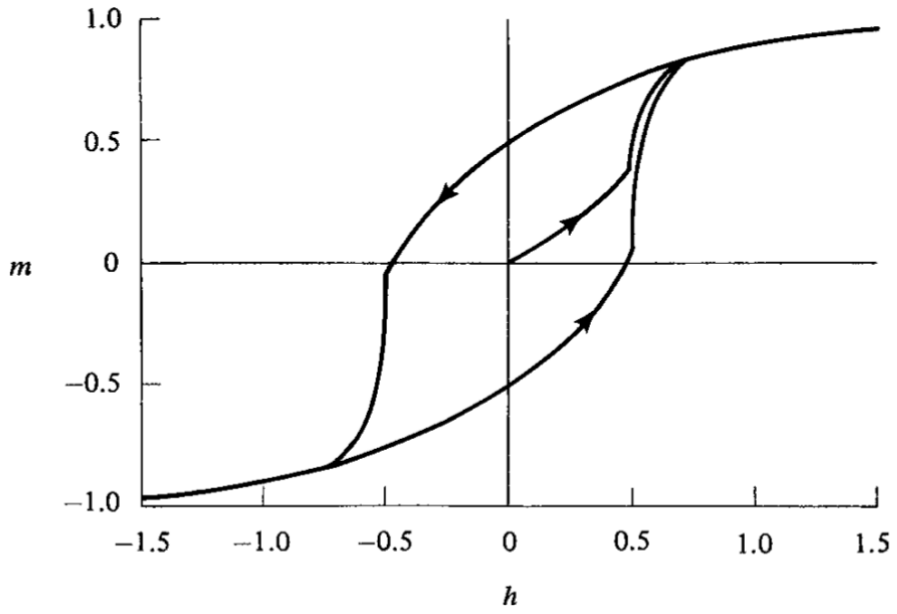

Figure 7: Hysteresis loop for an isotropic system of non-interacting single domain particles with uniaxial anisotropies oriented randomly in three dimensions [15].

The condition that particles must be non-interacting is a drastic approximation, as by ignoring the dipolar field from surrounding particles a significant contribution to the field on each particle is neglected. The work presented here treats the particles as in the random Stoner-Wohlfarth case, with uniaxial particles randomly oriented in 3-D. However, also included in the calculation are distributions of anisotropy strength K, particle size V, and interaction effects.

2.5 Effect of a Switching Field Distribution

The switching field required to reverse the magnetisation of a system of particles is a complex parameter. It is affected by the distribution of volumes of the particles, and the variations in anisotropy constant and direction. Also important is the existence of interactions between the particles due to dipolar forces. The width of the switching region or the differential of the hysteresis loop gives a measure of the distribution of values, the switching field distribution (SFD).

All systems of magnetic nanoparticles have a distribution of particle diameters which is usually lognormal of the form given in equation 21. Here D is the mean diameter of the particles in the system and σ is the standard deviation of $\ln(D)$. The lognormal distribution function of the diameter leads to a lognormal distribution function of the particle volumes given in equation 22.

$$f(D)\mathrm{d}D = \frac{1}{\sqrt{2\pi}\sigma D}\exp\frac{-\ln(D)-\overline{\ln(D)}}{2\sigma^2} \tag{21}$$

$$\sigma_{\ln(V)} = 3\sigma_{\ln(D)} \tag{22}$$

The field at which reversal occurs is then also distributed over a range of values as each individual particle has a different H_c. The practical difficulties involved in manufacturing particles with uniform diameter at the nanoscale mean that any real system of particles such as a frozen ferrofluid will have a large switching region.

In addition the value of uniaxial anisotropy constant is also distributed mainly due to variations in shape or saturation magnetisation. For systems with uniaxial crystal anisotropy, variations in the crystalline anisotropy constant K_c arise due to impurities, defects, or surface effects that may be of the same order as K_c. For particles with uniaxial shape anisotropy, variations in shape give rise to a similar distribution.

A further source of switching field distribution is the effect of dipole-dipole interactions. The net interaction field varies wildly and cannot be represented by a mean field. Hence, large scale numerical models are required. The effect of interactions is discussed in section 2.8.

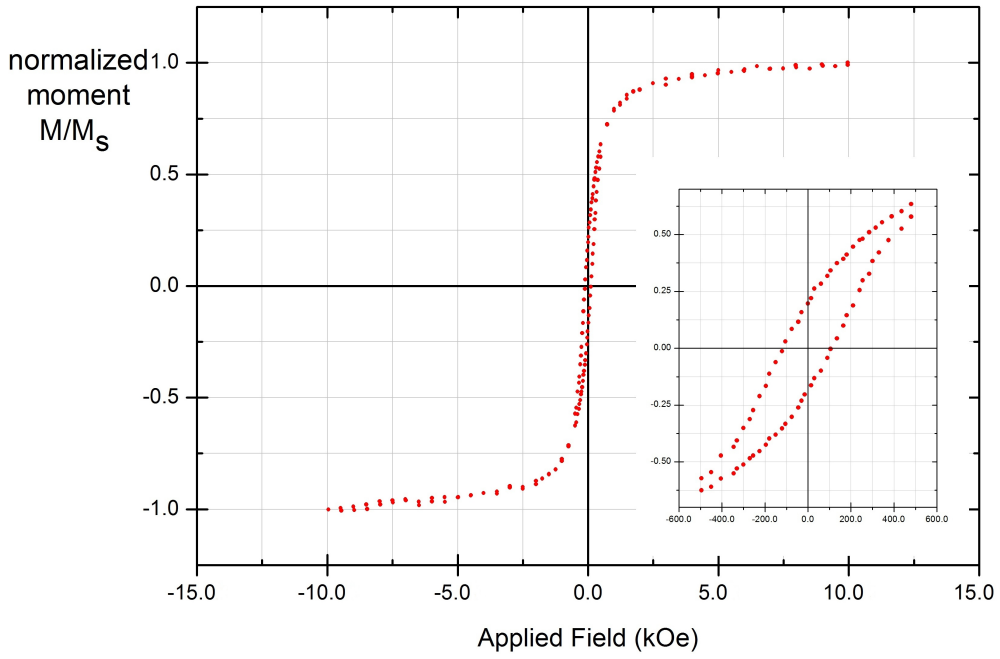

Figure 8: A hysteresis loop for an iron powder suitable for hyperthermia in a biomedical application [18].

The combination of these effects result in a wide switching field distribution approximated by the width of the switching region in the hysteresis loop. Figure 8 shows a typical experimental measurement of a hysteresis loop for a powder suitable for hyperthermia in a biomedical application. Here coercivity is $100\,Oe$ and the width of the switching region is approximately $800\,Oe$, or $8H_c$ [18].

Independent of its origin the behaviour of a distributed system can be described in terms of $f(\Delta E)\,\mathrm{d}\Delta E$,

a function of the energy barriers in the particles. $f(\Delta E)\,\mathrm{d}\Delta E$ gives the probability of finding a barrier between E and $E + \Delta E$. The barrier will be lowered by the application of a field. Such a distribution must be normalise to unity as below.

$$\int_0^\infty f(\Delta E)\,\mathrm{d}(\Delta E) = 1 \tag{23}$$

The remanence in a system depends on the degree of alignment of the easy axes and lies between 0.5 and 1.0 in the absence of thermal activation. The ratio M_r/M_s is usually called the loop squareness. It is limited by non-alignment of the easy axes that gives rise to a reversible component of the magnetisation.

$$\frac{M_r}{M_s} = M_r^{\max} \int f(\Delta E)\,\mathrm{d}(\Delta E) \tag{24}$$

The coercivity is a much more complex factor since it requires a balance of regions magnetised in different directions, including any form of reversible magnetisation [19].

2.6 Thermal Activation

The internal energies of a system of particles at $T \neq 0$ follow the Boltzmann distribution, and the moment of a single domain particle at $T \neq 0$ is subject to thermal fluctuations. It follows then that in an originally saturated system placed in zero field and where the energy barrier to reversal is $\Delta E = KV(1 - H/H_K)^2$, some particles may reverse instantaneously and some may reverse after a time t due to the influence of thermal fluctuations.

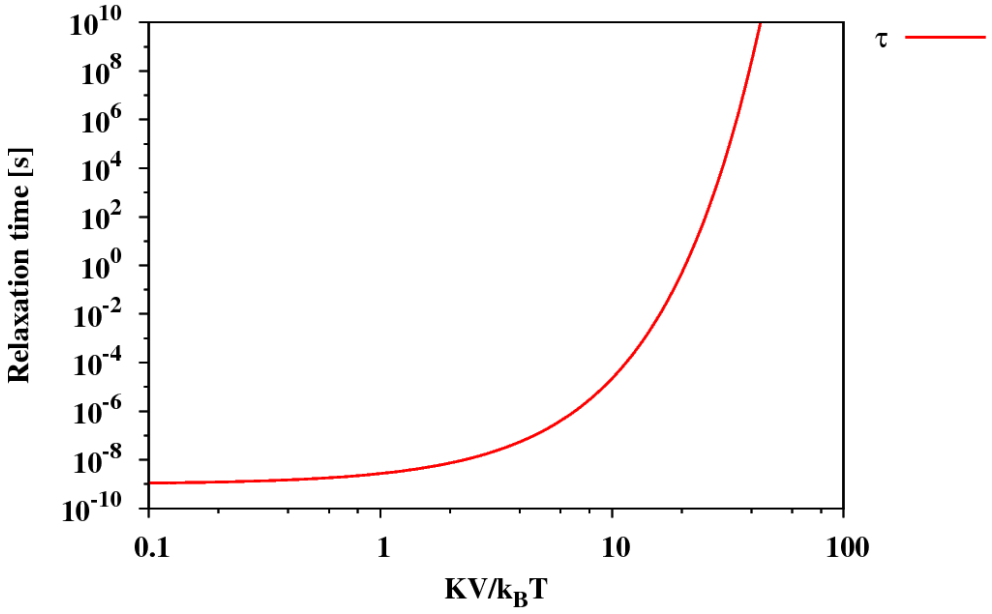

Figure 9: A plot of equation 25 using $H = 0$ with K and T constant. The Neel relaxation time ranges from nanoseconds to centuries depending on the volume of the particle.

The Neel relaxation time is the time taken for the magnetisation of a previously saturated system of identical particles to fall to $1/e$ or 37% of its initial value. It is denoted by τ_N and calculated using the Arrhenius-Neel Law (eqn. 25) [20]. Here k_B is the Boltzmann constant and f_0 is called the attempt frequency, which for ferromagnets is taken to be $10^9 s^{-1}$ based on calculations for iron by Kneller [21]. The variation of the relaxation time increases exponentially with particle volume, shown in figure 9.

$$\tau_N^{-1} = f_0 e^{-\Delta E/k_B T} \tag{25}$$

$t = 100\,s$ can be defined as a critical measurement time over which if the particle has a net magnetisation it is considered stable [22]. This is because $100\,s$ is roughly the time required in order to measure the remanence of a sample. Also, because the energy barrier is in the exponent, it will not be sensitive to variations in t. Using this value for t gives $\ln(tf_0) = 25$, and therefore rearranging equation 25 finds the critical energy barrier for the transition from superparamagnetic to thermally stable behaviour (eqn. 27).

$$\Delta E = KV\left(1 - \frac{H}{H_K}\right)^2 = \ln(tf_0)k_B T \tag{26}$$

$$\Delta E_c = 25 k_B T \tag{27}$$

In superparamagnetic particles $KV \sim k_B T$, the anisotropy energy is equivalent to the thermal energy so in zero field there is no energy barrier. Hence the magnetic moment of the particle are buffeted constantly by thermal fluctuations and cannot maintain a consistent direction of magnetisation. The magnetisation of superparamagnetic particles is governed by the same expression as that for paramagnets. The Langevin function (eqn. 28) treats a particle as an integral over the energy of all individual magnetic moments, which are in thermal equilibrium at T with an energy distribution according to Boltzmann. Here $\zeta = \mu H/k_B T$, where μ is a single magnetic moment.

$$L(\zeta) = \left(coth(\zeta) - \frac{1}{\zeta}\right) \tag{28}$$

Defining superparamagnetism by the size of the energy barrier in the particle leads to practical difficulties in parameterising real nanoparticles, especially in a mixed sample. Size is a much easier property to measure. Substituting $\Delta E = KV$ (when $H = 0$) in equation 27 leads to a critical volume for the stability of uniaxial particles, shown in equation 29. Alternatively, for uniaxial particles of constant size there will also be a temperature T_B known as the blocking temperature, below which the magnetisation will be stable.

$$V_c = \frac{25 k_B T}{K} \tag{29}$$

$$T_B = \frac{KV}{25 k_B} \tag{30}$$

It has been shown that the energy barrier is modified by an applied field, hence the distribution of energy barriers is a complex function. Figure 10 shows the shape of the distribution function and the regions of distinct behaviour which contribute to it. Equation 31 describes the three regions as integrals over $f(\Delta E)$ [19].

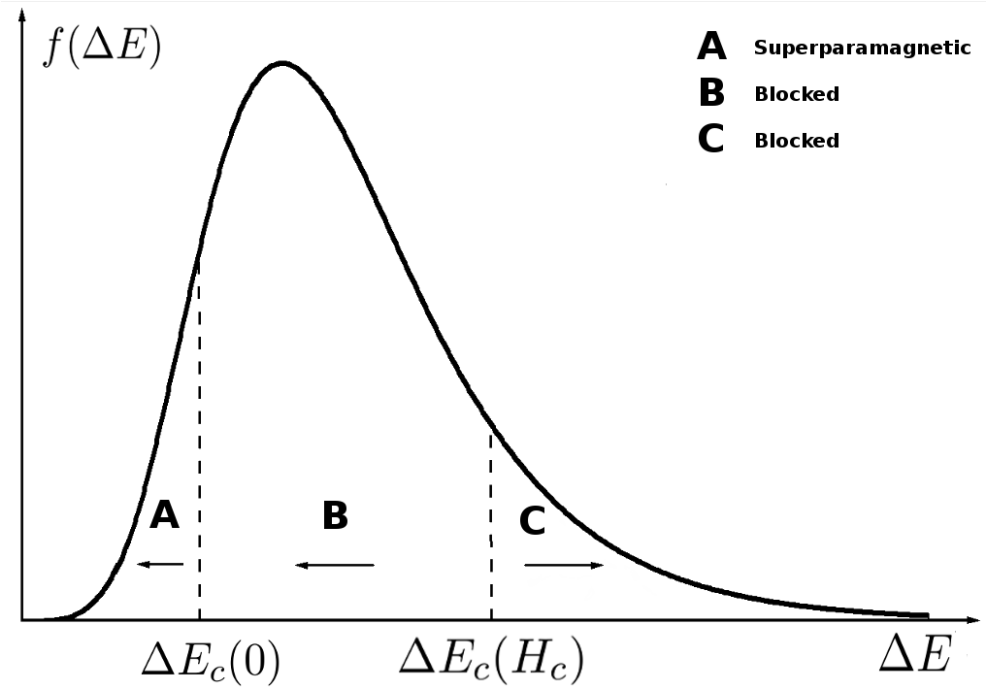

Figure 10: The distribution of energy barriers can be divided into three sections which categorise the types of behaviour.

$$\int_0^{\Delta E_c(0)} L(\zeta) f(\Delta E)\,\mathrm{d}(\Delta E) + \int_{\Delta E_c(0)}^{\Delta E_c H_c} f(\Delta E)\,\mathrm{d}(\Delta E) = \int_{\Delta E_c(H_c)}^{\infty} f(\Delta E)\,\mathrm{d}(\Delta E) \tag{31}$$

Each value of ΔE has an exponential decay. Time dependence can now be seen to occur at the value of ΔE_c that is active, but many discreet values of ΔE will be active around ΔE_c. This sum of exponentials lead to a variation of M which is linear in $\ln(t)$ (eqn. 33) [23].

$$M(t) = M(0) - S\ln(t) \tag{32}$$

$$\frac{dM}{d\ln(t)} = -S(H) \tag{33}$$

Since there are a different number of particles at varying values of ΔE, the rate of logarithmic decay S varies with field. It passes through a maximum at the peak of the distribution at a field generally close to H_c.

2.7 Frequency Dependent Effects

Hysteresis Losses

The time dependence of the magnetisation when an alternating field is applied leads to a frequency dependence of hysteresis loss. From the Sharrock law (eqn. 34) [24] it is possible to find an analytic solution for the coercive field H_c. The Sharrock law makes some simplifications and is only valid when the particles are not interacting and all the easy axes are aligned with the applied field.

$$H_c(t) = H_K \left(1 - \sqrt{\frac{k_B T}{KV} \ln\left[\frac{t f_0}{0.693}\right]}\right) \tag{34}$$

As the Sharrock law also assumes a static external field, in order to investigate frequency dependent effects it has first to be modified for an alternating field. It has been shown previously that the stepped field and swept field processes are related by the expression in equation 35 [25], where t_{eff} is the effective time to be used for t in equation 34 and $R = \mathrm{d}H/\mathrm{d}t$ is the field sweep-rate. It follows that coercivity must be dependent on the rate of sweep of the field, which is given in equation 36 [26]. Here $h_c = H_c/H_K$.

$$t_{\text{eff}} = \frac{k_B T}{KV} \frac{R^{-1} H_K}{2(1 - H_c/H_K)} \tag{35}$$

$$H_c(R) = H_K \left(1 - \sqrt{\frac{k_B T}{KV} \ln\left[\frac{k_B T}{KV} \frac{f_0 H_K}{2(1-h_c)} \frac{1}{R}\right]}\right) \tag{36}$$

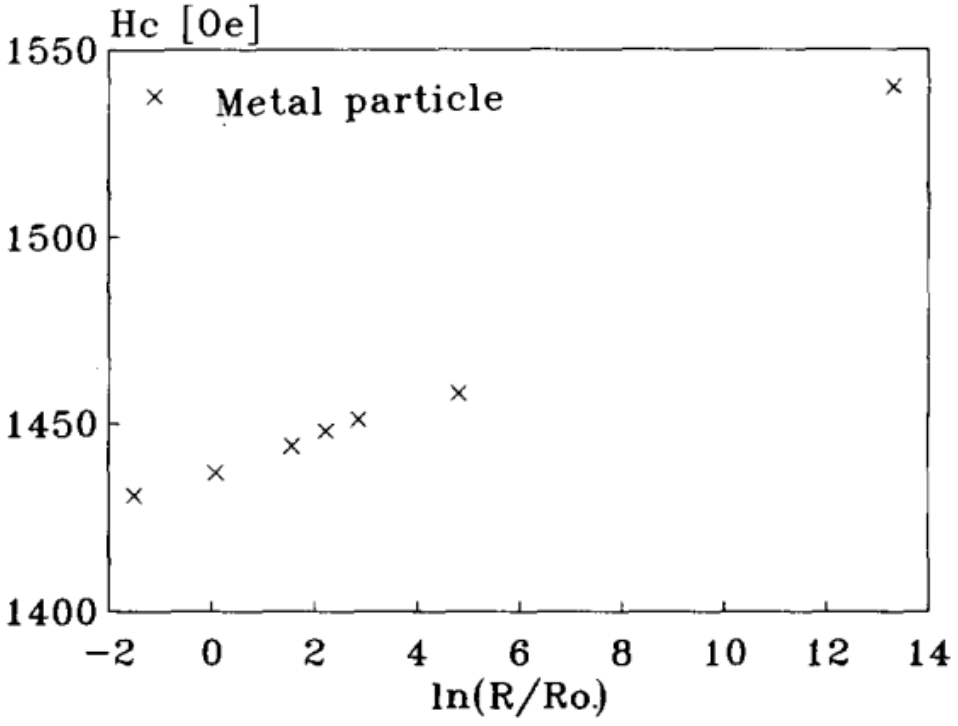

Figure 11: Coercivity plotted against sweep-rate for metal particle tape shows the increase in H_c as frequency increases [27].

Figure 11 uses a logscale for the measurement times used to find the coercivity range over 16 decades [27]. The scale is normalised to R_0, the initial sweep-rate. For low sweep-rates the coercivity increases linearly with $\ln(R/R_0)$, but this trend does not continue as R increases. This is because for high sweep-rate f_0 is a limiting factor as $t \to 10^{-9}$.

The remanence and the coercivity are both increased at high sweep-rate, increasing loop squareness. Therefore the hysteresis losses are proportional to the square of the frequency. The frequency of an alternating applied field is therefore a critical parameter in controlling the amount of heat produced from hysteresis losses, as shown in figure 12. For higher frequency sweeps of the applied field, a greater proportion of the larger superparamagnetic particles have a relaxation time longer than the time taken for each sweep of the loop. The loops for these higher frequencies are then wider as more particles contribute to the hysteresis losses by exhibiting thermally stable behaviour.

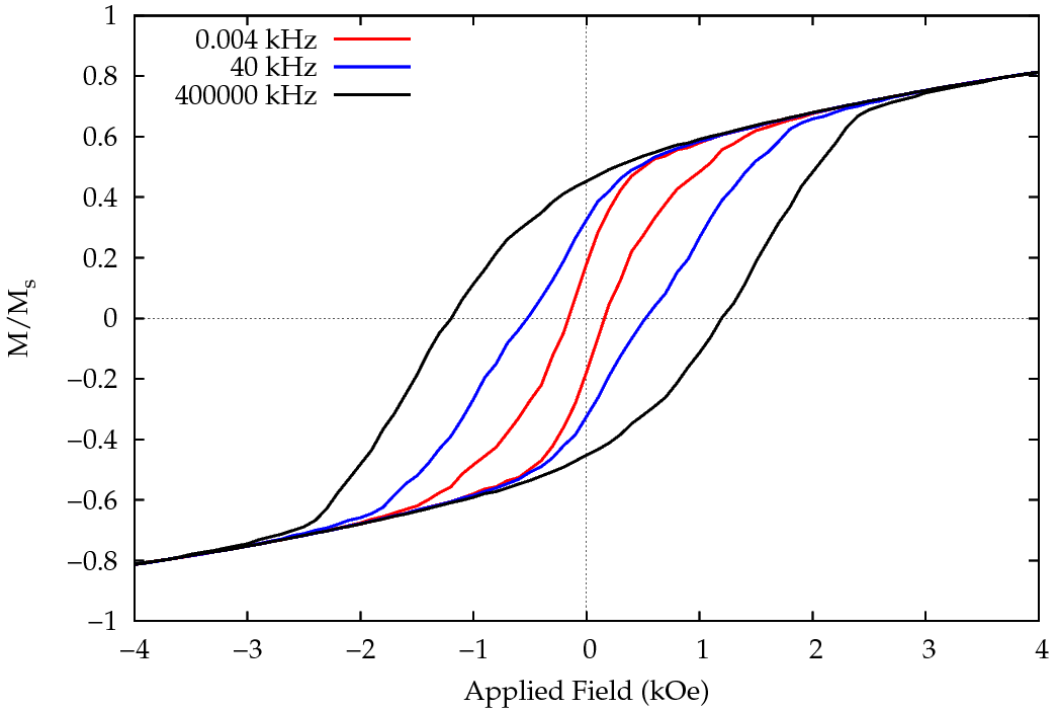

Figure 12: Calculated curves for 7.5 nm iron particles showing the expansion of the loops at high frequencies, where a greater proportion of the particles exhibit hysteresis.

Other Losses

Particles in a fluid can rotate physically to align their moments with an applied field, this also releases energy as heat. Whether or not rotation occurs depends on the size of the particles, V, and the temperature T and viscosity η of the fluid in which they are dispersed. The minimum size at which particles can undergo Brownian rotation is given by the Shliomis diameter (eqn. 37) [28].

$$D_S = \sqrt[3]{\frac{24k_BT}{\pi K}} \tag{37}$$

The Brownian rotation of the particles has a characteristic relaxation time, τ_B, given in equation 38. The radius r_h is the hydrodynamic radius of the particle, which is often larger than the radius of the magnetic volume. These losses occur at fields low enough to allow the particles to physically rotate before the Neel relaxation causes the magnetisation of the particle to flip. The two relaxation times combine to give an effective time, τ_{eff}, where usually one mechanism is dominant (eqn. 39) [29].

$$\tau_B = \frac{4\pi\, r_h^3 \eta}{k_B T} \tag{38}$$

$$\tau_{eff} = \frac{\tau_N \tau_B}{\tau_N + \tau_B} \tag{39}$$

Particles suspended in a colloidal ferrofluid have been shown to have greatly reduced heating when Brownian relaxation is prevented [30]. When injected into a tumour it is reasonable to suppose that the ability of the particles to move freely will be reduced by sticking to or possibly entering the cells. The model used in this experiment treats the particles as frozen in position, therefore Brownian losses are unable to contribute to the heating and are not considered.

The electrical conductivity of the particles induces eddy currents at the surface of the particle when a changing field is applied. Eddy currents produce heat due to the resistance of the material, but they also work to limit the penetration of the field into the particle, resulting in lower hysteresis and susceptibility losses. Fortunately eddy currents have been shown to be negligible for small particles (less than 100 nm in diameter) if the frequency of the the alternating field is also less than $10\,GHz$ [31]. At very high field strengths eddy currents can be generated in the human body itself, causing non-specific heating in healthy areas that are not intended to be damaged. The product of the maximum field and the frequency must be $H_{max} f < 6.10 \times 10^6\, Oes^{-1}$, and the frequency $f < 1.2\,MHz$, in order to prevent inductive heating of the surrounding tissues in the patient or stimulation of nerves or cardiac muscles, which are both painful and dangerous [32].

Susceptibility, χ is a measure of how responsive a material is to an applied field, it has real and imaginary components χ' and χ'' respectively. The imaginary component of the susceptibility is equivalent to the energy released as heat. When a particle is subject to an alternating external field susceptibility losses occur because the moments in an alternating field oscillate in order to stay aligned with the field. Susceptibility losses occur at all field strengths, and are proportional to the frequency. At high frequencies the moments lag behind the actual direction of the field because they are unable to rotate fast enough to keep up. This causes a loss peak in χ'' and the heat produced, as shown in figure 13 [33].

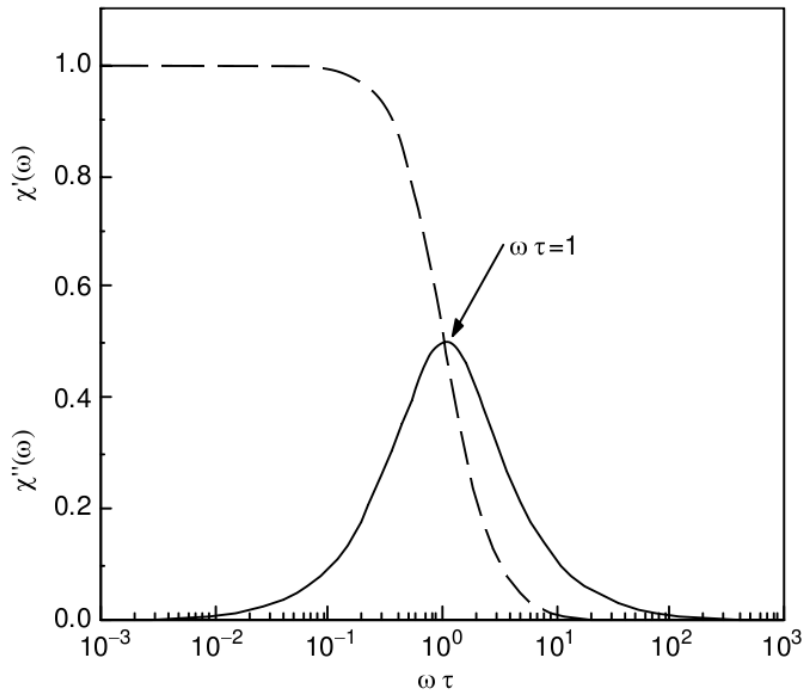

Figure 13: A modelled curve; the maximum possible imaginary component χ'' is half that of the real component χ'. Here $\omega = 2\pi f$ and the curves are normalised to the maximum frequency [33].

2.8 Interaction Effects

Two types of interaction affect particulate or granular systems. The first is the dipole-dipole field which is demagnetising overall but at close separation can be magnetising. The second is the exchange interaction, which is strongly magnetising but has short range and is very sensitive to the distance between moments. The exchange interaction dominates in systems such as thin films, where grains are close packed and have $\sim 100\%$ concentration. In general dipolar interactions reduce the overall remanence of the sample. H_c has complex variation but broadly is reduced according to equation 40, where ϵ is the packing fraction and is between 0 and 1 [34].

$$H_c(\epsilon) = H_c(0)(1 - \epsilon) \tag{40}$$

In the types of powder systems used for hyperthermia the packing fraction is very low, such that the concentration of iron is between $5 - 10\, mg/ml$ [32]. Hence exchange interactions can be discounted. In principal dipolar coupling will also be negligible but particle aggregation gives rise to local concentrations where the effects will be significant. Therefore interactions can have noticeable effects on the parameters of the hysteresis loops produced by fine particle systems. It has been shown that interactions lead to a reduction in the saturation remanence [35], but the effect on coercivity is more complex.

The original Sharrock law neglects interactions but can be modified to take account of the dipole

field by calculating effective terms for H_K and KV. Using the modification given in equation 35 for a swept field and fitting to calculations of H_c for 3-D randomly distributed systems leads to the following expression for an effective energy barrier [36]:

$$\Delta E_{\text{eff}} = (KV)^{\text{eff}} \left(1 - \frac{H}{H_K^{\text{eff}}}\right)^2 \tag{41}$$

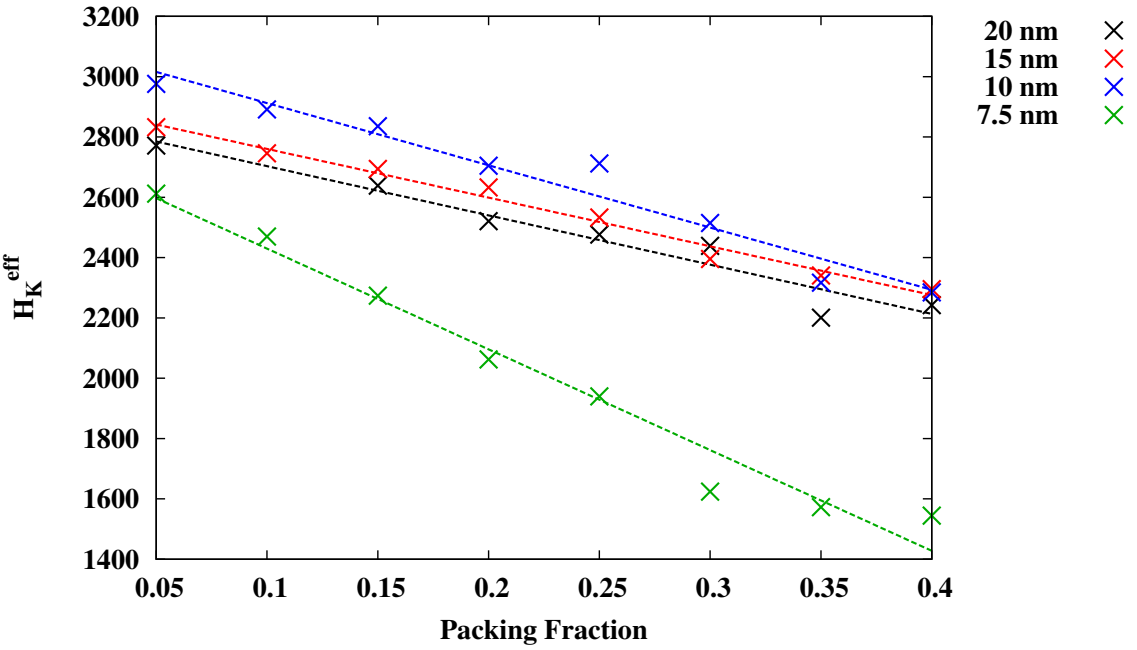

Figure 14: Effective H_K is reduced at higher packing densities as a result of interaction effects from surrounding particles, the effect is more pronounced for smaller particles.

Figure 14 shows that the value of the fitted parameter H_K^{eff} decreases for higher packing fractions, where each particle will be subject to interactions with an increased number of neighbouring particles. However for systems of small mean particle diameter, ie with a significant proportion of superparamagnetic particles, the reduction of H_K^{eff} is not the dominant effect. For these systems, interactions have been shown to increase the coercivity at low frequencies [36].

Typical concentrations of magnetic material in fluids used in clinical trials are low, containing approximately $100\, mg_{Fe}/ml$ [14]. Assuming the nanoparticles are made up of pure magnetite this concentration equates to a packing fraction in the liquid of about 0.016. However, with the improvement of targeting techniques it is likely that the particles can be concentrated in the tumour tissue resulting in more nanoparticles per ml than in the fluid, and consequently more particles will contribute to produce a greater heating effect.

3 MAGNETIC HYPERTHERMIA

3.1 Basis of Magnetic Heating

As discussed in section 2.7 there are 4 mechanisms of heating in magnetic particles; Brownian rotation, eddy current heating, susceptibility loss, and hysteresis loss. The mechanism which occurs is dependent on the particle size V, but it is uncertain which mechanism is typically characteristic of any particular size. As detailed earlier both hysteresis loss and Brownian rotation have critical sizes that can be calculated and below which these mechanisms do not act. Eddy current heating only occurs in particles larger than $100\,nm$ for frequencies below the GHz range [31]. In any system where V is distributed it is likely that more than one mechanism occurs in any one sample.

The type of heating is also dependent on the environment in which the sample is located. For example, a small particle encased in a polymer sphere will be unable to physically rotate thus removing any component of heat produced via Brownian motion. Whereas for a system of aggregated particles the relevant hydrodynamic radius will be that of the cluster, consequently particles smaller than the Shliomis diameter may be able to physically rotate [37].

Recently there has been both experimental and theoretical research looking into the contribution of each mechanism to the heating of magnetic nanoparticles, as well as the effect of particle size and size distribution of samples on the heating contribution of each mechanism [29] [38] [39] [40]. Irrespective of the mechanism, there are many reports of work undertaken to measure the total heating effect in different systems [41] .

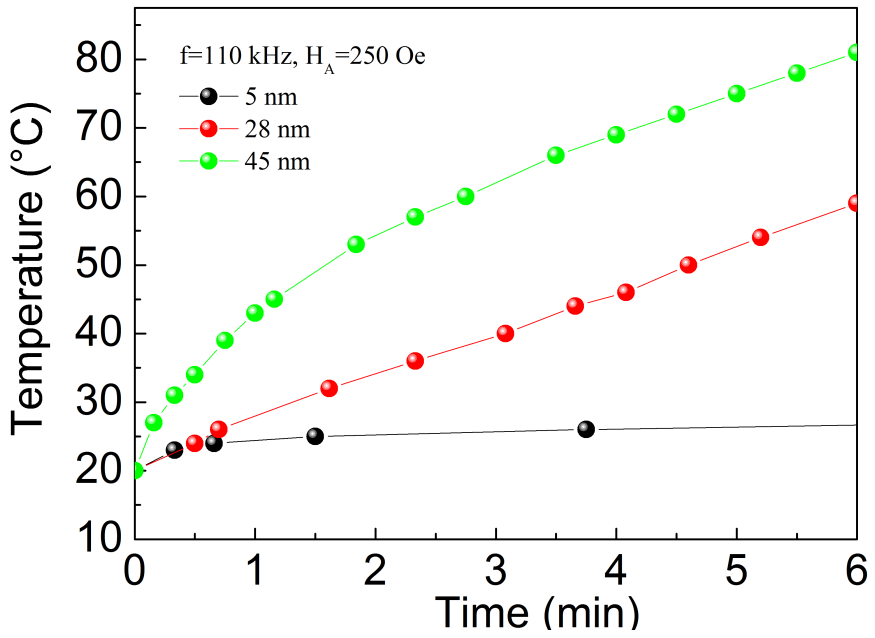

Figure 15: Measured heating curves for systems with varying mean diameter [18].

Figure 15 compares experimental data for the rate of heating of three systems with differing median particle diameters subject to the same applied field strength and frequency [18]. It is clear that for the system of small particles very little heating occurs as almost all particles are below the critical sizes. However, for the two larger systems the initial rate of heating is larger for the larger particles and after approximately 3 minutes reduces to become almost equal to the heating rate of the middle system, as the curves become more parallel.

This suggests the same mechanism is dominant in both larger systems at this point, but the larger system is also affected by a second heating mechanism at the initial time. It is believed that the initial heating rate of the green curve is due to susceptibility losses, which are complex as the particles are both multidomain and aggregated. The dominant mechanism for the red curve and after a finite time for the green curve is linear, and this is believed to be due to the Brownian rotation of the aggregate because for particles above the Shliomis diameter in a liquid environment Brownian losses dominate [42].

When considering a system of aggregate particles, simple analytical models are insufficient to accurately describe the behaviour of the sample. For realistic solutions a numerical integration is necessary over all the particles in the system that considers how each particle is affected by its position relative to all the other particles with which it is interacting. Rosensweig [43] has derived a frequency dependent expression for the total power loss per unit volume of magnetic material and implemented it in a theoretical model of some ferrofluid systems.

$$P = fE_H = \pi\mu_0\chi'' f H_{max}^2 \tag{42}$$

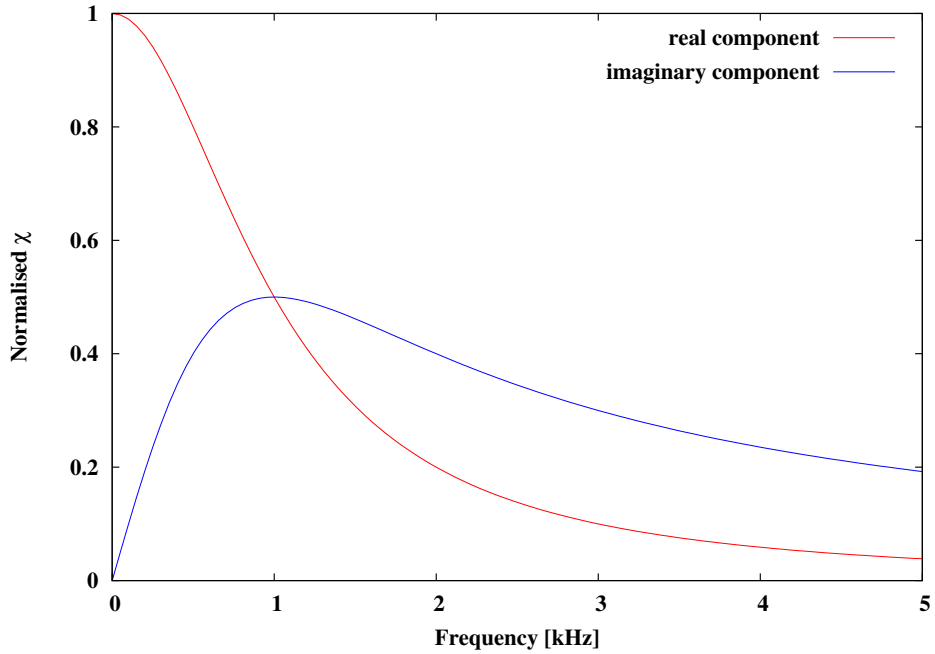

Figure 16: Real and imaginary components of the complex susceptibility for a system of particles with no size distribution, calculated using equations 43 and 44

Recall that χ'' is the imaginary component of the susceptibility and is relative to the susceptibility loss heating. Figure 16 shows the frequency dependence of the real and imaginary components of the complex susceptibility χ for a system of particles with uniform size. The curves are normalised to the equilibrium susceptibility χ_0, on which χ' and χ'' depend as defined below. χ_0 itself is variable with applied magnetic field.

$$\chi =' \chi_0 \frac{1}{1 + (2\pi f \tau_{\text{eff}})^2} \tag{43}$$

$$\chi'' = \chi_0 \frac{2\pi f}{1 + (2\pi f \tau_{\text{eff}})^2} \tag{44}$$

Here τ_{eff} is the combined relaxation time of Neel and Brown given above in equation 39, maximum heating occurs when the Brown relaxation dominates in this term. When χ'' is substituted in equation 42 above an analytically solvable expression for the power dissipated in one second by susceptibility and Brownian losses is found.

$$P = \pi \mu_0 \chi_0 f H_{max}^2 \frac{2\pi f \tau_{\text{eff}}}{1 + (2\pi f \tau_{\text{eff}})^2} \tag{45}$$

In a comparison of heating rates of different materials (fig. 17) the two 'softest' materials as characterised by their relatively low anisotropies, magnetite (Fe_3O_4) and maghemite (γ-Fe_2O_3), produced peak heating rates over a third higher than cobalt ferrite and over twice as high as barium ferrite. The diameters of the particle systems which produced these high heating rate were also significantly larger than the diameters corresponding to the $CoO{\cdot}Fe_2O_3$ and $BaO{\cdot}6Fe_2O_3$ peaks. The optimum diameters were approximately $7\,nm$ and $8\,nm$ for barium and cobalt ferrite respectively. The peak for magnetite was at $\sim 14\,nm$ and for maghemite $\sim 20\,nm$; below these diameters the particles would tend to become superparamagnetic, and so the amount of heating would become minimal.

The rate of heating in figure 17 is related to the anisotropy strength of each material and the dependence of V_c on K in equation 29. Even though the minimum particle sizes for these materials to produce any heat are larger than particle sizes in a stable colloid, other requirements for some clinical uses of nanoparticles will mean that they will be encapsulated in a polymer shell limiting aggregation.

The systems were modelled as monodisperse particles, i.e., with standard deviation of particle size $\sigma_D = 0$. The effect of a lognormal distribution of size dispersion was introduced in calculations for magnetite and shown to have a significantly detrimental effect on the heating rate. The peak heating rate was reduced from $\sim 700\,K/s$ to $\sim 400\,K/s$ when the standard deviation of size distribution σ was increased from 0 to 0.05. However, an incredibly fast heating rate such as this is inappropriate for clinical application in any case. If the heating is not carefully controlled there is a severe risk to the patient of burns and damage to healthy tissues.

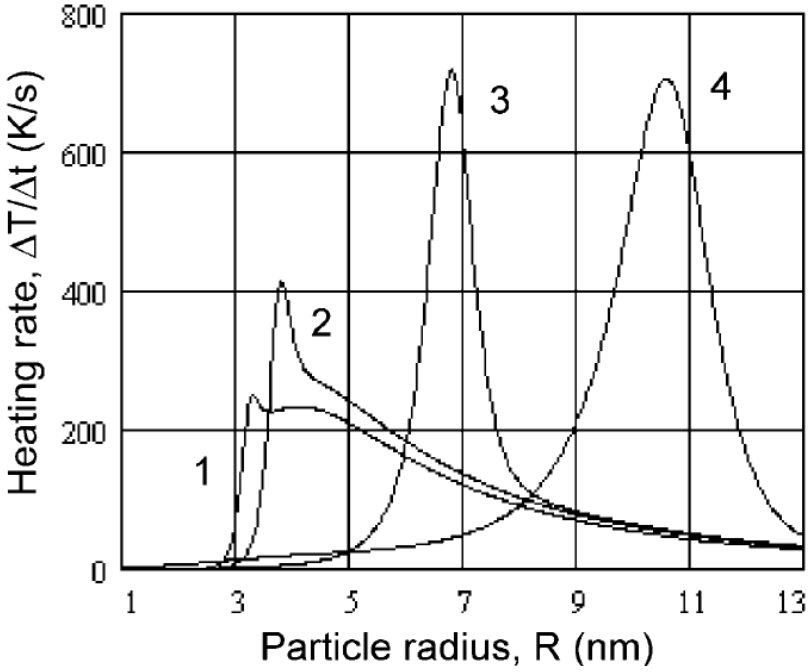

Figure 17: Curves showing heating rate against particle radius for 1. $BaO{\cdot}Fe_2O_3$, 2. $CoO{\cdot}Fe_2O_3$, 3. Fe_3O_4, and 4. γ-Fe_2O_3 [43].

3.2 Materials and Equipment

In order to produce significant heat output whilst limiting the strength and frequency of the field it would be preferable to use one of the more strongly magnetising materials such as cobalt. Unfortunately many magnetic materials are highly toxic to humans. This problem is compounded by the reactions of nanoscale particles in the human body, which are not fully understood. In fact it has been found that even usually inert materials such as gold can have detrimental effects when introduced into the body for certain sizes of nanoparticle [44].

Currently the only magnetic material that has been found to be biocompatible and approved for use in humans is magnetite. The enhanced toxicity of other nanoparticles is for the moment unlikely to be overcome. However it is possible that in the future the use of more strongly magnetic materials coated in an inert shell will be an option for hyperthermia treatment [45]. There is research ongoing into the effects of core-shell interactions on the magnetic properties of nanoparticles [46].

In the early days of nanoparticle manufacturing for use in ceramics and powder metallurgy industries many particles were produced by grinding large specimens into finer and finer powder, a process known as milling [47]. Now there are many methods of chemically building nanoparticles through deposition or nucleation, allowing the characteristics to be tailored to specific requirements. These include small particles diameters with very narrow size distributions. Magnetic nanoparticles have also been combined with other materials producing systems with applications in

sensing, biocatalysis, targeted infection, magnetic resonance imaging, and drug delivery [48]. Figure 18 shows an image taken with a transmission electron microscope of a single layer of γ-Fe_3O_4 particles in a ferrofluid with very uniform diameters of $\sim 11\,nm$ [49].

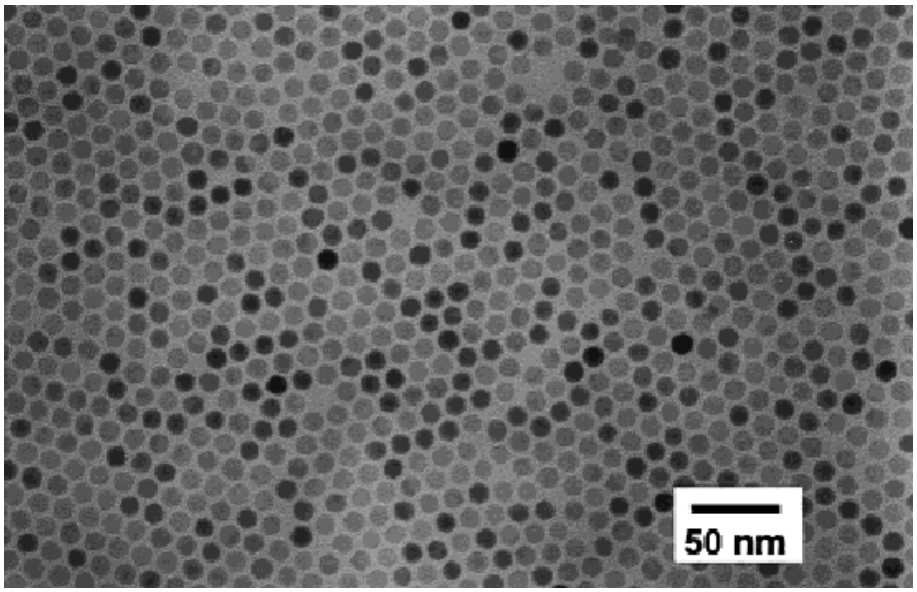

Figure 18: TEM image of 2-D assembly of $11\,nm$ diameter γ-Fe_2O_3 nanoparticles with narrow size distribution [49].

Nanoparticles can be manufactured to the necessary standards for use in clinical trials, but a method of field generation is also required. For small scale usage commercial bench-top hyperthermia devices are available which have frequency ranges of $50\,kHz$ to $1.2\,MHz$ with field strengths up to $250\,Oe$ [50]. These systems can be used in particular to insert plasmids or other biological material into cells via a magnetic nanoparticle carrier, which is much less harmful to the cell than injection or other methods.

This sort of equipment is unsuitable for use in humans on a clinical scale. Patients may require treatment on organs located deep within the body, such as the liver, and to generate a homogeneous field over a large area requires a more powerful field generator. Alternative methods of heating have been trialed such as radiofrequency waves, microwaves, and ultrasound, but all of these have the limitation of being unable to target the tumour sites specifically and also suffer inhomogeneous temperature distribution due to difficulties penetrating uniformly through body tissues.

Clinical studies of magnetic hyperthermia were begun by Jordan et al. [10] at Charité University Hospital in Berlin in 2000. The alternating field generator machine designed and built there for treatment of humans is shown in figure 19. It has a ferrite core to boost the field strength output and is capable of a field frequency of $100\,kHz$ for field strengths up to $225\,Oe$ over a vertical treatment space of $30 - 45\,cm$ in which the patient must lie.

Figure 19: The MAG-300F alternating field generator at Charité University Hospital, Berlin [12].

Since then, many trials have investigated the suitability of magnetic nanoparticles for treating particular types of cancers using in vitro and animal studies. Studies of the amount of heating produced by differently manufactured nanoparticles and the best coatings for stability in vivo have been undertaken in rats. More recently, phase I and II clinical trials have been conducted in humans and the effectiveness of magnetic hyperthermia as both a stand-alone treatment and in conjunction with surgery, radiotherapy, and chemotherapy has been evaluated [51].

3.3 Applications

Studies have shown that rats are a good model for the evolution of malignant glioma in humans. This is a type of aggressive brain tumour which is currently untreatable [52]. A study of magnetic hyperthermia in rats with glioma, using coated magnetite particles in field strengths up to $225\,Oe$ at $100\,kHz$ produced temperatures inside the tumours of $43 - 47°$ which could be finely adjusted by tuning the field strength. These temperatures caused areas of necrosis in the tumours and life expectancy of the rats increased up to 4.5 times that of the control group for the highest temperatures [11]. For cases in humans where no other treatment method is viable, or has failed it may be possible to use hyperthermia as a palliative treatment, extending life expectancy or the quality of life without causing the detrimental side-effects associated with chemotherapy.

As an isolated treatment magnetic hyperthermia cannot guarantee complete destruction of all tumour cells due to the difficulties involved in ensuring uniform particle, and consequently temperature, distribution throughout an irregularly shaped tumour. As a result of areas with lower particle concentration there may be cool spots within the tumour which can survive the treatment and be undamaged so that they can continue to replicate. The nature of cancer being uncontrolled cell division this will then cause a recurrence of the tumour. However in the case of slow growing and most importantly benign tumours such as those which cause enlargement of the prostate gland, magnetic hyperthermia has been used as an alternative to repeated surgical intervention.

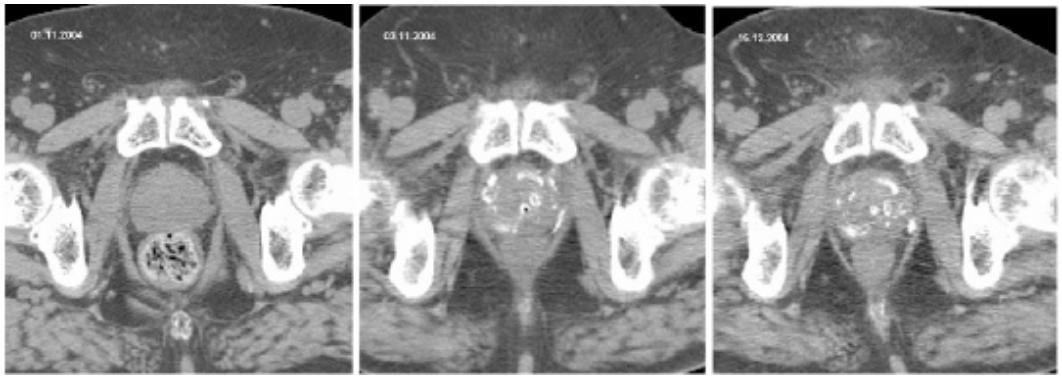

Figure 20: CT scan of a cancerous prostate gland before, immediately after, and 6 weeks after magnetic hyperthermia therapy. Image reprinted from [12].

The first report on clinical application of interstitial hyperthermia using magnetic nanoparticles in the treatment of human cancer was published in 2005 [12]. Figure 20 shows a computerised tomography image from that paper of a prostate gland containing a benign tumour before and after magnetic hyperthermia treatment. The magnetite particles remained stable in the prostate for the full six weeks of treatment and did not require subsequent 'top-up' injections.

Hyperthermia has also been shown to improve the clinical outcome of patients simultaneously undergoing radiation therapy [3]. If used correctly, hyperthermia not only causes an additive effect, but can work synergistically with the standard treatment. The optimum timeframe is thought to involve radiation first followed $3-4$ hours later by hyperthermia [53]. For this particular application, temperatures of $41.5-43°C$, referred to as 'mild temperature hyperthermia' are employed. These temperatures do not kill most types of cell directly but DNA repair is often inhibited for a short time after the treatment which prevents cells previously damaged by radiation from successfully recovering and replicating. Another factor in the improved response is the sensitisation of cells that are normally resistant to radiation, such as those in a low pH environment or in the process of replicating. The first of these conditions is very common inside tumours due to poor circulatory systems caused by unregulated growth which is itself due to the cancerous cells continually replicating.

3.4 Future Developments

Future developments in hyperthermia for the treatment of malignant diseases and other tumours are likely to be in the areas of improving functionalisation of nanoparticles to better target only certain types of cell and only cancerous cells of that type. Research into this is being undertaken by the MULTIFUN project [54], which has brought together experts in biomedicine, oncology, and chemistry from research groups, hospitals, and companies that manufacture nanoparticles. The goal of MULTIFUN is to develop magnetic nanoparticles designed for 'theragnostics': combining diagnosis and imaging of tumours with multiple methods of targeted therapy.

This involves attaching biological molecules to nanoparticles which cause them to accumulate in tumour tissue. Once there the magnetic properties allow the particles to perform as contrast agents to pinpoint tumours in MRI imaging. If the particles are injected intravenously this method could potentially highlight secondary tumours that have spread to other parts of the body while they are still small. When a tumour is confirmed the dose of functionalised nanoparticles can be increased as necessary. The application of an alternating magnetic field will then apply targeted heating which can simultaneously sensitise the cells and trigger the release and activation of anti-cancer drugs. Figure 21 shows the three separate mechanisms that can be achieved with functionalised nanoparticles.

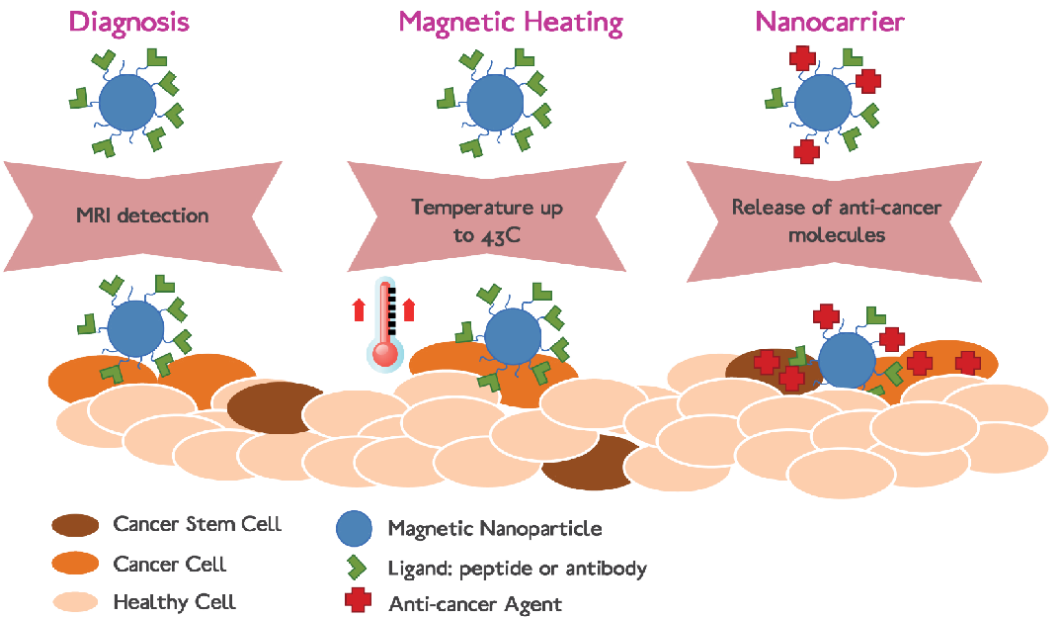

Figure 21: The three applications of functionalised magnetic nanoparticles being researched by the MULTIFUN project [54]

3.5 Objectives of this Work

Clinical trials on both rats and humans have demonstrated hyperthermia therapy as proof of concept for particular forms of cancer. However, due to the wide variations in how quickly the same type of cancer grows and spreads, and the differing degrees of response to any treatment in different people, large sample sizes are required to accurately assess the effectiveness of the treatments. As a result of this experiments on animals tend to only compare 2 or 3 sets of parameters alongside a control group. Theoretical studies can help focus practical experiments by exploring a wide selection of magnetic materials, as well as changing the parameters of the nanoparticles and the applied field, to find biologically viable combinations of these which produce the greatest heat output for the most economical input conditions, without the expense and bureaucracy of performing clinical trials.

The purpose of this project was to investigate the optimum parameters for generating the maximum amount heat from hysteresis losses in biologically compatible nanoparticles. To this effect the behaviour of a variety of systems of randomly dispersed nanoparticles made of iron-based magnetic materials were simulated for a number of different particle diameters and packing fractions while the systems were subjected to an alternating field over a range frequencies and maximum field strengths.

4 SOFTWARE METHODS AND DEVELOPMENT

4.1 Principle of the Model

The system considered in this experiment is a sample represented by a cubic cell of interacting single domain particles with periodic boundary conditions. A lognormal distribution characterises both the diameter and the anisotropy constants of the particles, which have standard deviations of 0.1. The anisotropy easy axes are also distributed randomly in three dimensions, as would be the case for a solidified colloidal ferrofluid. The simulation is supposed to be useful to compare with experiments and medical trials, consequently the temperature used throughout is body temperature, $310\,K$.

The highest percentage of magnetic material contained in a unit of colloidal ferrofluid is $\sim 15\%$, since if further concentration is attempted the particles will tend to aggregate [42]. The concentrations of magnetic material that can be safely injected into a human being are much lower than the technical limits of ferrofluid density. This is especially true if the substance is intended to circulate in the bloodstream rather than be injected directly into the tumour site. Despite the low densities at injection, the state of the system within the tumour may well be much higher as particles accumulate at the targeted site. Consequently the densities investigated here are between 5% and 40% to account for the possibility of non-colloidal states in vivo.

The assembly of nanoparticles is modelled with a kinetic Monte-Carlo algorithm which takes into account the behaviour of both superparamagnetic and thermally stable particles. For the mean diameters considered in this case (5-20 nm) there will be a non zero fraction of superparamagnetic particles [55].

This model makes use of the Mersenne Twister [56], a random number generator well suited to Monte-Carlo algorithms as they require a very large sequence of unique random numbers. The Mersenne Twister has a period of $2^{19937} - 1$ and passes many tests for statistical randomness.

Two mechanisms are used to calculated the probability of magnetic reversal P_r, depending on whether the particle is classed as superparamagnetic or thermally stable. Thermally stable particles defined by the parameter $KV > k_B T ln(t f_0)$ are treated as Stoner-Wohlfarth particles with two energy minima. In order to account for thermally activated switching a probability of switching between minima proportional to the magnitude of the energy barrier is included. Otherwise, for particles where $\Delta E < 3k_B T$ the energy barrier is so small that the two-state approximation is invalid. The direction of the moment must be considered able to point in any direction and the probability of it being found in a particular direction is derived from the Boltzmann distribution.

4.2 Initialisation of the Particle Array

Figure 22 shows an example of the initialised particle system. It is impossible to produce this arrangement through random assignment of particle co-ordinates at high packing densities because the probability of particles overlapping becomes too high. The method used here is based on creating a system initially of low packing fraction and then shrinking to the required concentration.

The size of the cubic cell is initially defined as having a length of $4\sqrt[3]{N}\,D$, where D is the median diameter and N is the number of particles in the simulation. This gives a low initial density and allows plenty of space for the particles to be placed in at random. The particles are assigned radii according to a lognormal distribution with $\sigma = 0.1$, and their random co-ordinates in the cubic cell are generated.

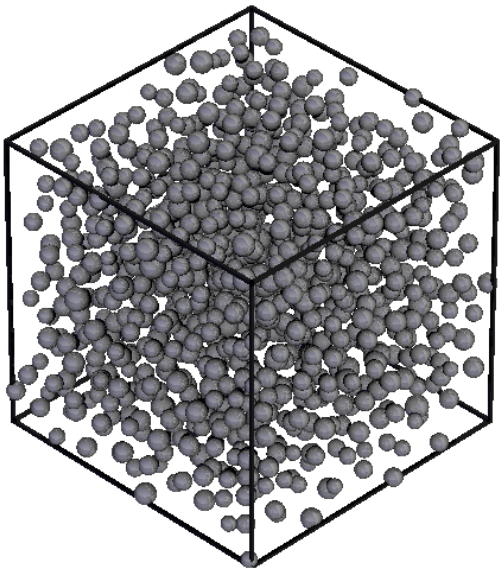

Figure 22: A visual representation of the arrangement of 1000 particles generated by the system initialisation code at 10% packing fraction produced using Povray, an image rendering program.

A neighbour list is drawn up which keeps track of where each particle is located in an array of sub-cells. This is to cut down on computational time when checking whether particles are touching or overlapping after they are moved. Each particle is checked only against the particles in the same and immediately neighbouring sub-cells.

The system is then checked for particles occupying the same space and if necessary expanded to remove overlaps. So that the system can be shrunk to the required density quickly the particles are encouraged to move apart by application of a repulsive potential. The energy E_i is quartic with respect to the magnitude of separation r_{ij} between the central co-ordinates of particle i and surrounding particles j.

$$E_i = \sum_{j \neq i} 1000 \times \left(\frac{d_m}{r_{ij}} \right)^4 \tag{46}$$

A Monte-Carlo algorithm moves each particle a small distance and compares the new energy to the old $\Delta E_i = E_{new,i} - E_i$. The new position of the particle is accepted if the particle has moved away from its neighbours $\Delta E_i < 0$. It is also accepted with a probability that decreases as ΔE_i increases by comparison to a uniformly generated random number, expressed as $\exp(-\Delta E_i) < [0, 1[$. Thus as the particles attempt to move closer together the potential energy is increased and the move is less likely to occur. As the moves are accepted the neighbour list is updated as necessary. This is repeated 50 times for each particle.

The smallest separation between any two particles is then calculated and the system is shrunk until those particles are almost touching. The Monte Carlo process is then repeated and the system shrunk again until the desired packing density is reached. A final run through the Monte Carlo process equilibrates the system. This algorithm efficiently produces random configurations for particle densities of up to 25% of the cubic volume for 8000 particles. The code which produces the initial configuration is included in the appendix.

4.3 Demagnetising the System

The initial state of the system is random, and so it is likely that the internal energy will not be minimised. When the hysteresis loop is generated the field strength begins at zero, so it is necessary to produce a realistic demagnetised state [57]. This is especially important when only minor hysteresis loops are generated, as in this case the net magnetisation of the system is not maximised at any point. Without initially demagnetising the system, the simulation could begin at zero field in a higher energy state than the maximum applied field would be able to produce in reality.

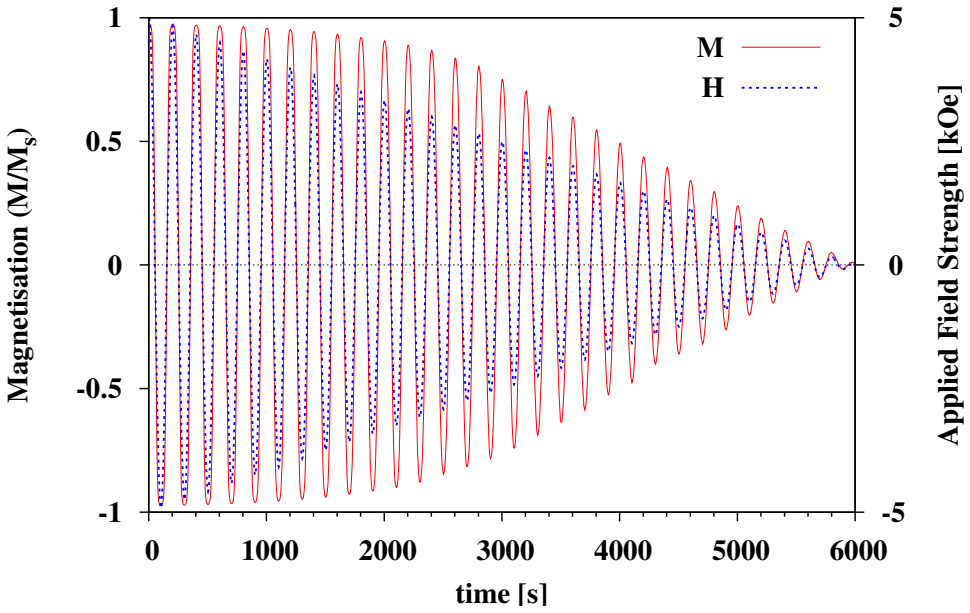

Figure 23: Curves showing the application of an alternating applied field (blue curve, right axis) which reduces over time drives the net magnetisation of 20 nm iron particles to zero.

To demagnetise the system a field of $5000\,Oe$ is initially applied. This is strong enough to almost magnetise a system of magnetite or iron particles. The field is slowly reversed, to allow the magnetisation of the system to follow closely and the maximum field strength is reduced at each cycle. As is shown in figure 23, after many cycles the system is left in a demagnetised state when the applied field and net magnetisation are reduced to zero.

4.4 Interaction Field

The dipolar interactions from surrounding particles results in a dipolar field which acts on each particle. This must be calculated and added to the external field to discover the total field acting on each particle. In equation 47 the local field H_{loc} is the vector sum of the dipolar interaction fields produced by the moments of surrounding particles μ_j on each particle i and the applied field H_{app}.

$$H_{\text{loc}} = \sum_{j \neq i} \left[\frac{3(\mu_j . r_{ij})}{r_{ij}^5} - \frac{\mu_j}{r_{ij}^3} \right] + H_{\text{app}} \tag{47}$$

Here the $1/r^3$ dependence leads to the contribution from each particle to the dipolar field diminishing rapidly as the separation distance between two particles, r_{ij} increases. Consequently, to conserve computational time the summation was calculated for all j within range to up to a cut-off radius $r < r_{\text{max}}$. A mean-field approximation for a spherical sample shape was used to calculate the contributions from particles outside this range. For these calculations r_{max} was set to be five times the median diameter of the particles.

4.5 Hysteresis Loop Calculation

Consider the method implemented on superparamagnetic particles. The moments of these particles exist in a thermal equilibrium therefore must be characterised by polar co-ordinates θ and ϕ. Consequently the energy of each particle i can be defined as a function of these angles where any angle is possible, and the field $E(\theta, \phi, H_{\text{loc}})$. The direction of the moment is then distributed according to Boltzmann statistics, with a probability for each state given by equation 48, where z is the partition function, which is equal to the sum of all the possible states ensuring that the maximum value for the probability P_i is 1.

$$P_i = \frac{1}{z} e^{-\Delta E_i / k_B T} \tag{48}$$

$$z = \sum_i e^{-\Delta E_i / k_B T} \tag{49}$$

The reversal probability of superparamagnetic particles defined by $\Delta E < ln(tf_0)k_BT$ is calculated using the Metropolis algorithm [58]. The Metropolis algorithm works by producing a new state for the particle with the moment at random values of θ and ϕ and calculating the energy difference with the previous state. If the new energy is lower than the original energy, i.e., $\Delta E < 0$ the new position is accepted. If $\Delta E > 0$ it is accepted with the probability defined in equation 50; if $\exp(-\Delta E/k_BT)$ is lower than a uniformly generated random number between 0 and 1 to which it is compared.

$$P_r = min(1, e^{-\Delta E/k_BT}) \tag{50}$$

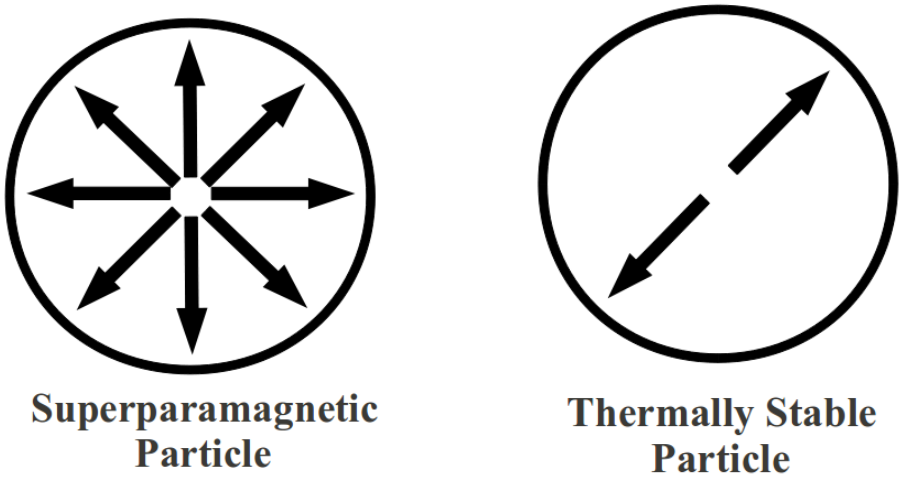

Figure 24: A schematic of the moments in single domain particles. Superparamagnetic particles can point in any direction, whereas thermally stable particles are restricted to two energy minima.

The difference between the allowed directions of the moments in superparamagnetic and thermally stable particles is shown in figure 24. For thermally stable particles as defined by $\Delta E > ln(tf_0)$ the Metropolis algorithm is inefficient because the probability of the moment being found anywhere other than close to the energy minima is extremely small. It would therefore take a long time to produce a realistic statistical distribution of moment probabilities. Consider instead then a simulation algorithm based on the Stoner-Wohlfarth particle theory. In this theory, the total magnetic moment of a particle is described by μ which is the product of the particle volume V and the saturation magnetisation M_s.

The energy of a single particle is given previously in equation 6 and produces two energy minima denoted by E_+ and E_-, aligned parallel and antiparallel with the anisotropy field respectively, and separated by an energy maximum E_0. Note that these energy values are magnetic field dependent. At certain threshold magnitude H_t one of the minima coincides with E_0; either $E_+ = 0$ or $E_- = 0$ depending on whether $HKcos(\psi) > 0$ or < 0, respectively. It has been calculated [59] that the threshold field is $H_t = H_K g(\psi)$, where $H_K = 2K/M_S$ is the anisotropy field and

$$g(\psi) = (\cos^{2/3}\psi + \sin^{2/3}\psi)^{-3/2} \tag{51}$$

Here ψ is the angle between K and H. Thus for field magnitudes $H < H_t$ there are two stable states and for $H > H_t$ there is one unique state. Accordingly a Stoner-Wohlfarth particle shows hysteresis when magnetisation M is plotted as a function of the field H. Thus switching of a particle between the two states occurs whenever the magnitude of $H_{loc,i}$ becomes equal to the threshold field $H_{t,i}$.

So far this method is entirely deterministic, which is suitable for particles with $\Delta E >> ln(tf_0)k_BT$. However, although many particles have energy barriers large enough to be modelled as a two-state system, they are also small enough to be influenced by thermal fluctuations.

Including the spontaneous reversal effect of thermal activation in the model requires probabilistic expressions, hence probabilities $P_{+,i}(t)$ and $P_{-,i}(t)$ are assigned for a particle to be in its '+' or '$-$' state at a given time t, respectively. The normalisation condition gives $P_{+,i}(t) + P_{-,i}(t) = 1$ for all values of t and the time evolution of these probabilities is governed by the master equation:

$$\frac{dP_{+,i}(t)}{dt} = -w_{+,i}(t)P_{+,i}(t) + w_{-,i}(t)P_{-,i}(t), \tag{52}$$

Here $w_{+,i}$ and $w_{-,i}$ are transition rates for moment transitions from '+' to '$-$' and from '$-$' to '+', respectively, and are related to the Neel relaxation time $\tau_N^{-1} = w_{+,i} + w_{-,i}$. The transition rates are assumed to take the Arrhenius form:

$$w_{\pm,i} = f_0 \exp\left(-\Delta E_{\pm,i}/k_BT\right) \tag{53}$$

The energy barriers are defined as $\Delta E_{\pm,i} = E_{0,i} - E_{\pm,i}$ with $E_{0,i}, E_{\pm,i}$ being the energies associated with the energy maximum and the two minima according to the discussion above. The smaller of the two energy barriers can be calculated using by the numerical Pfeiffer approximation [59].

$$\Delta E(\psi_i, H_{loc,i}) = K_iV_i\left[1 - \frac{H_{loc,i}}{g(\psi_i)}\right]^{\kappa(\psi_i)}, \tag{54}$$

Here $g(\psi_i)$ is given by equation 51 and the exponent $\kappa(\psi_i) = 0.86 + 1.14g(\psi_i)$. With these definitions, equation 52 can be solved in a straightforward manner under the assumption of constant external field H, which implies time independent rates $w_{\pm,i}$, and

$$P_{\pm,i}(t) = w_{\mp,i}\tau_N\left(1 - \exp\left(-t/\tau_N\right)\right) + P_{\pm,i}(0)\exp\left(-t/\tau_N\right) \tag{55}$$

τ_N is the characteristic relaxation time associated with the particle i, and $P_{\pm,i}(0)$ are the initial values for probabilities at time $t = 0$. For long times $t \to \infty$, and equation 55 leads to equilibrium solutions where $\Delta E_{\pm,i} = E_{0,i} - E_{\pm,i}$.

$$P_{\pm,i}(\infty) = w_{\mp,i}\tau_N = \frac{e^{-\Delta E_{\mp,i}}}{e^{-\Delta E_{+,i}} + e^{-\Delta E_{-,i}}} = \frac{e^{-E_{\mp,i}}}{e^{-E_{+,i}} + e^{-E_{-,i}}}, \tag{56}$$

Thus, according to equation 55, if a particle i is initially in the state '$+$', for example, which implies $P_{-,i} = 0$ and $P_{+,i} = 1$, the probability that this particle can be found in the '$-$' state after the time Δt is $P_{-,i}(\Delta t) = w_{+,i}\tau_N\left(1 - \exp\left(-\Delta t/\tau_N\right)\right)$, and similarly for the opposite switching event starting from the initial state $P_{-,i} = 1$ and $P_{+,i} = 0$. Thus, the condition for finding the particle moment in the opposite state after time Δt can be expressed by equation 57, where $P_i(\infty)$ is given by equation 56 depending on the initial state.

$$P_i(t) = P_i(\infty)\left(1 - \exp\left(-\Delta t/\tau_N\right)\right), \tag{57}$$

Given the consideration above, we can formulate the computational algorithm to follow the time-evolution of the magnetisation state as a sequence of the following rules:

1 Assuming external field is H at time t, increment the field to be $H' = H + \Delta H$ at time $t' = t + \Delta t$.

2 Pick a particle i and find '$+$' and '$-$' states by the energy minimisation of equation 6 when subject to $H_{\text{loc},i}$.

3 Calculate $E_{0,i}$, $E_{\pm,i}$, $\Delta E_{\pm,i}$ from equation 54 and $w_{\pm,i}$ using equation 53.

4 Evaluate probability $P_i(\Delta t)$ of switching during the time interval Δt according to equation 57.

5 Generate a random number between 0 and 1 according to a uniform distribution and switch the particle i if $r > P_i(\Delta t)$, otherwise do nothing.

6 Update the local fields $H_{\text{loc},j}$ acting on neighbours of a particle i according to equation 47.

7 Go to step 2 and repeat steps 2-7 N times until all particles have been chosen.

8 Go to step 2 and repeat steps 2-8 N_{mcs} times, where N_{mcs} is the number of Monte-Carlo steps. This is essential for averaging.

9 Set $H = H'$ and $t = t'$. Return to step 1 and continue until a hysteresis loop is generated.

Thus the sequence of steps 1-8 defines the particle state evolution during the time interval $\delta\ t = \Delta\ t\ N_{\text{mcs}}$, which can be thought of as the time interval during which the external field is incremented by ΔH. This allows the definition of the external field rate as $R = \Delta H/\delta t = \Delta H/(\Delta t N_{\text{mcs}})$.

4.6 Extracting information from the loops

To find the coercivity the hysteresis loop data was analysed and the equation describing the straight line joining the first two points found either side of the zero axis was calculated. From this the value of H at the point where that line crosses zero was determined. This finds the first time that the magnetisation goes below zero and so for a hysteresis curve with lots of noise, such as one describing a minor loop, this method will underestimate the true coercivity. However, when considering minor hysteresis loops the coercivity is not a particularly useful property, as the reduced squareness of minor loops renders the estimation of the area given by the coercivity inaccurate.

To find the area of the loop the values of the magnetisation were increased, a shift of $+1$ ensures the loop has only positive values for M/M_s. Treating the upper and lower curves separately the difference in the area was found by numerical integration of each curve using the trapezoidal rule. This method requires the integrand to be described by a sequence of equally spaced points. The error is proportional to $1/n^2$, where n is the number of points used to evaluate each curve.

The energy lost as heat through one complete cycle of the field has been described as a function of the hysteresis loop area previously in equation 1. However, as the field can alternate over a large range of frequencies a more useful measure is the energy dissipated in a set amount of time, the power:

$$P = f M_s \int M dH \tag{58}$$

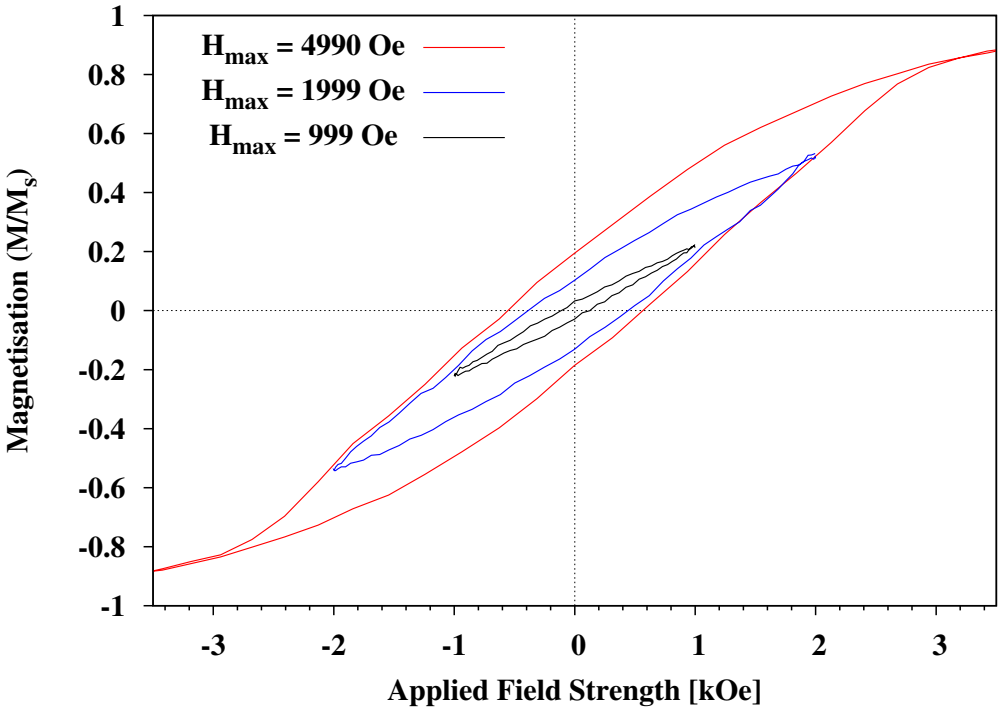

Figure 25: A comparison of hysteresis loops produced for different values of H_{max} on an iron composite.

The integral goes from H_{max} to $-H_{max}$. The effect on the heat output of the range of the field is shown in figure 25. Here the frequency used for the three loops is the same, but the maximum applied field is only strong enough to fully magnetise the sample and complete the hysteresis loop for the blue curve. Both the red and black curves form minor loops with correspondingly lower values of M_r and H_c because the demagnetising dipolar field which is produced by the unmagnetised fraction at $H_{\text{max}} = 1\,kOe$ and $H_{\text{max}} = 2\,Oe$ is contributed to by 80% and 50% of the particles in the sample respectively.

In summary a model has been developed to generate a system of interacting magnetic fine particles and calculate the heating due to hysteresis when an alternating magnetic field is applied. This allows the amount of hysteresis heating produced by different materials and system parameters to be investigated, as well as the effects of dipolar interactions on the amount of hysteresis heating. The model can also be used to calculate the frequency dependence of the hysteresis heating, leading to a value of optimum frequency for heating a given system.

5 RESULTS

5.1 Properties of fine particle magnetic systems

The hysteresis losses generated by interacting fine-particle systems are governed by many competing factors which effect the shape of the hysteresis loop. Those due to the intrinsic properties of the material are the anisotropy K and the saturation magnetisation M_s. The physical arrangement of the system is defined by the median volume of the particles V_m which are distributed lognormally, as well as the packing fraction ϵ. The characteristics of the applied field are the maximum value H_{max} and the sweeping-rate H_{rate} or frequency f. The strength of interaction effects in the system also influences the loop shape and is itself a complex combination of some of the factors already mentioned, the equation for the interaction energy is:

$$E_i = \frac{\vec{\mu} \cdot \vec{\mu}}{r^3} = \frac{M_s V_1 \times M_s V_2 cos(\theta)}{r^3} \tag{59}$$

The strength of the interaction effect is dependent on three separate parameters. Firstly the square of the saturation magnetisation M_s; as an example the saturation magnetisation of iron is approximately four times larger than that of magnetite, $M_s = 1710\, emu/cc$ and $470\, emu/cc$ respectively. This means that the strength of interactions in a system of iron particles compared to that between magnetite particles is ~ 16 times stronger. The size of the particles $V_{1,2}$ will be calculated from the lognormal distribution around the median particle diameter with a standard deviation $\sigma = 0.1$. Finally, the distance between the particles r, which will be represented by the packing fraction ϵ as an average for the whole system; r will decrease proportionally when packing fraction increases.

The interaction field is demagnetising overall and in places can be very strongly demagnetising, but individual particles may exist in a position where demagnetising contributions from surrounding particles cancel out, or in regions where the local field is magnetising. Since particle interactions are a function of distance, it has been stated that systems with 0.05 packing fraction can be considered to behave as though they are non-interacting [36], however this is only the case when the smallest r, the distance to the nearest particle is approximately the same for all particles, i.e., the particles are arranged in a lattice structure. When particles are arranged randomly they tend to clump together, consequently interactions inside clusters of particles are significant even when the packing fractions are as low as 0.001 [42].

5.2 Interactions: Dependence on particle size

The proportion of superparamagnetic particles in a system is known to influence the width of the hysteresis loop. When the median diameter D_m is large, a greater proportion of the particles will be thermally stable because the distribution of D_m is lognormal. It follows that for any particular field sweeping-rate, hysteresis losses will increase non-linearly as the median particle size increases until all particles contribute to the loss.

For this simulation a system of cobalt particles was chosen due to its high anisotropy which results in a strong variation in the loops with grain size. Hexagonal close packed cobalt has a uniaxial anisotropy constant of $4 \times 10^6\, ergs/cc$ and M_s of $1400\, emu/cc$, and requires a field of at least $\sim 4\, kOe$ to saturate it. A field strength of less than this would result in the formation of minor loops, which would have other effects on the loop shape and area and make it more difficult to observe the effect of particle size. Therefore the maximum field used was $5\, kOe$ and the frequency was $200\, Hz$. The critical diameter for the transition to superparamagnetic behaviour can then be calculated from the equation for critical volume V_c, equation 29.

$$D_c = 2\sqrt[3]{\frac{3}{4\pi}V_c} \tag{60}$$

From this equation, the critical diameter for the above parameters is found to be $6.7\, nm$. Systems with D_m between 5 and $20\, nm$ were investigated, and so it is expected that the $5\, nm$ system exhibits primarily superparamagnetic behaviour although the tail of the lognormal distribution will mean that some particles will be blocked. It is also expected that the $20\, nm$ system will contain a majority of thermally stable particles. The systems investigated have a packing fraction of 0.05 and the temperature used was body temperature, $310K$.

$$H_c = H_K \left[1 - \left(\frac{\ln(tf_0)k_BT}{KV}\right)^{1/2}\right] \tag{61}$$

As shown in figure 26 the shape of the loop varies greatly when the median particle diameter is close to the superparamagnetic limit. The coercivity increases from $30\, Oe$ for the system with the smallest particles to $2.3\, kOe$ for the larger particle system. The increase in coercivity as the median diameter is increased from very close to the superparamagnetic limit is non-linear. From equation 61 the size dependence of H_c can be seen to be proportional to $\sqrt[2]{V}$, and the rate slows as the maximum possible H_c is approached. As the particle diameter increases beyond the limiting size for single domain behaviour they will break up into multiple domains and therefore total volume is no longer a relevant size parameter.

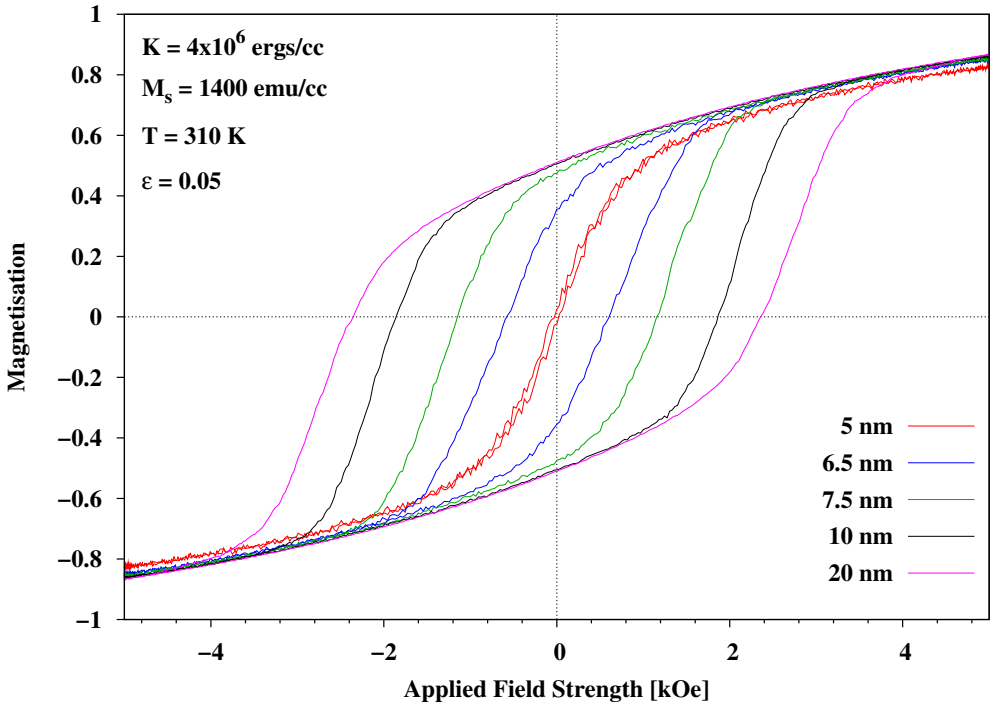

Figure 26: Hysteresis comparison of cobalt particles with different median diameters.

5.3 Interactions: Effects of packing fraction

From equation 59 it can be seen that the separation distance has an effect on the interaction strength. The average separation is not measured, but it is known to decrease as packing fraction increases since packing fraction is calculated from $V_{\text{all particles}}$ divided by $V_{\text{cubic cell}}$, and the cubic cell was 'shrunk' over more iterations to generate systems with higher packing fractions. In systems where the average separation distance is lower a greater number of particles will be included inside the cut-off radius for calculating interactions, so the effect of interactions on the systems should be enhanced by increasing the packing fraction.

For this simulation the parameters used are those for iron since it has the highest magnetisation, thereby better illustrating the effect of interactions. The systems compared have packing fractions of 0.05 and 0.2. The saturation magnetisation of iron is $1710\,emu/cc$, and the cubic anisotropy constant is $4.2 \times 10^5\,ergs/cc$. The model assumes a uniaxial anisotropy, but for particles of iron the crystalline anisotropy is not strong enough to overcome the effect of shape anisotropy due to the nanoscale size of the particles. This changes the anisotropy from cubic to uniaxial and applies to particles under $40\,nm$ in diameter [60] so the model is applicable in this case. The median diameter of the system of particles was $20\,nm$, temperature was $310\,K$, the frequency of the alternating field was $1\,kHz$ and the maximum field strength was $1\,kOe$.

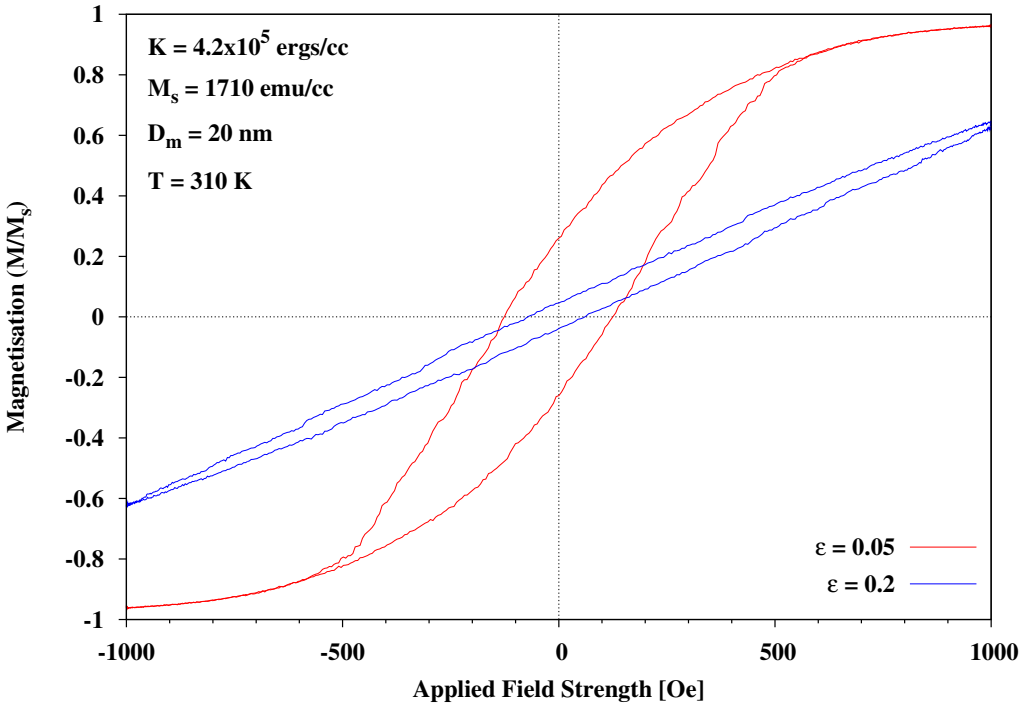

Figure 27: Hysteresis loops of different densities of 20 nm diameter iron particles with field alternating at a frequency of 1 kHz.

Figure 27 shows the hysteresis loops produced by this simulation. The interactions lower the gradient of curve, which indicates overall they have a demagnetising effect and the interaction field opposes the applied field. The area of the loop is reduced because generally both H_c and M_r are reduced by interactions. However, the effects are often complex and an increase in H_c is possible under certain circumstances. This is because the local micromagnetic configurations can be magnetising or demagnetising depending on the magnetic history of the sample.

For this system the saturation field is increased significantly; the sample only reaches 60% saturation in a 1 kOe field and therefore a minor loop forms which reduces the coercivity as well as the remanence. For the 5% by volume sample a fully closed loop forms at a field less than 1 kOe but for the 20% by volume sample the loop does not close and only 0.6 M_s is achieved in a field of 1 kOe. This indicates that the effective overall dipolar field is demagnetising and of the same order as the applied field.

On average the largest particles will be the last to be magnetised, and they will have the largest interaction effect on other particles. Consequently, when the applied field is removed the large particles which retained their opposing magnetisation will impose a significant demagnetising field on the reversible particles and some of these are flipped, greatly reducing M_r. The result of this simulation shows that interactions have very strong effect in systems of iron particles.

The same experiment as above was performed with the same system parameters, except with K and M_s values representing magnetite. The cubic anisotropy of magnetite is $1 \times 10^5\, ergs/cc$ and saturation magnetisation is $470\, emu/cc$, again the anisotropy can be assumed to become uniaxial for small particles. Interaction effects on magnetite systems should be less strong than those for iron because the saturation magnetisation of magnetite is ~ 4 times smaller. From equation 59 the strength of interactions in magnetite are therefore ~ 16 times weaker than in iron.

The effect of interactions in a system of magnetite particles is shown in figure 28, the saturation field is increased as in iron but saturation is still achievable at fields lower than $1\, kOe$ and a full hysteresis loop is able to form, therefore a meaningful comparison can then be made between the two systems of different packing fraction. The gradient of the curve is reduced by a much lesser degree than for iron as a result of the lower saturation field. Interactions widen the loop by increasing the coercivity from $36\, Oe$ to $66\, Oe$, correspondingly increasing the area.

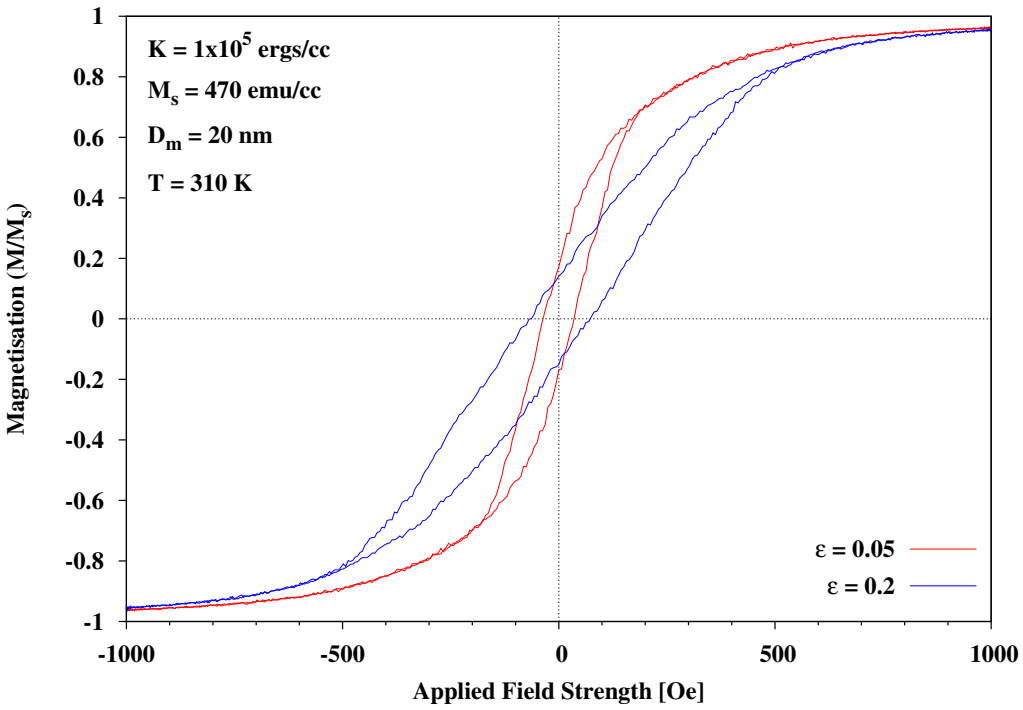

Figure 28: Hysteresis comparison of different densities of $20\, nm$ diameter magnetite particles with field alternating at $1\, kHz$.

The remanent magnetisation is slightly lowered by interactions, this is because at the remanence the only field acting on the particles is the dipolar interaction field, and at higher packing fractions there are more neighbouring particles contributing to this field. When there are only a few neighbouring particles some of them will couple to produce particle-pairs, these pairs reinforce each others magnetisation. Whereas at high packing fractions there are large clusters of particles all contributing to produce a stronger local field which gives rise to localised areas of zero net mag-

netisation by forming closed loop structures. Figure 29 shows a diagram of the arrangement of the two types of structure.

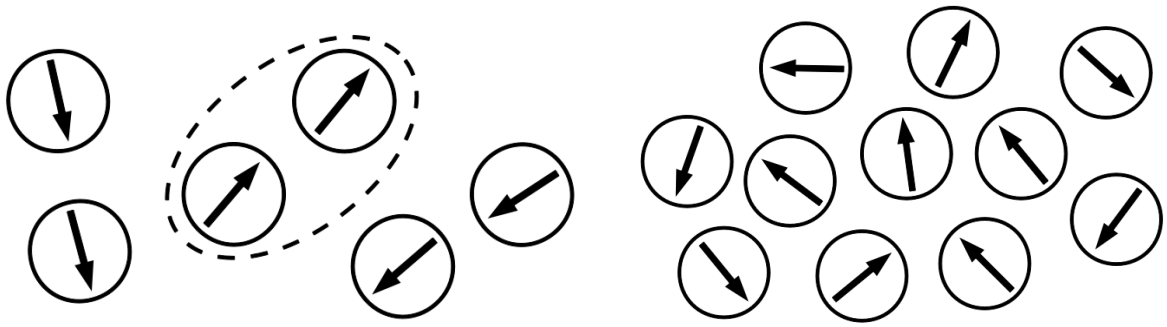

(a) (b)

Figure 29: (a) Systems with low packing fraction arrangements result in the formation of particle pairs. (b) Particles in densely packed arrangements form closed loop structures.

5.4 Interactions: Dependence on M_s

In principle the hysteresis loss over one cycle of the alternating field is governed by the values of H_c and M_s, therefore an increase in the M_s should result in a greater heating effect. In order to confirm this the hysteresis loops of two otherwise identical systems with differing saturation magnetisations have been compared. An anisotropy of $2 \times 10^3\, ergs/cc$ was chosen, which is a typical value for a soft magnetic material such as nickel-iron. The M_s values chosen were $1910\, emu/cc$ and $860\, emu/cc$, these are representative of FeCo and NiFe respectively [16].

The toxic nature of these particular materials would necessitate polymer encapsulation if used in vivo, but there are applications within industry where toxicity is irrelevant, such as glue softening, for which they could be suitable. As for the other parameters; median particle diameter of the systems was $20\, nm$, packing fraction was 0.05, and the field frequency was $1\, kHz$.

Figure 30 shows the comparison of the hysteresis loops for systems defined by the parameters discussed above. The graph is normalised with respect to the saturation magnetisation, so for otherwise identical systems it could be expected that the shape of the two curves ought to be approximately the same. However, it is clear that M_s influences the shape of the loop in a more complex manner. The gradient of the curve with lower M_s is much steeper indicating it is correspondingly easier to magnetise with only small fields, here 50% saturation is reached in half the applied field strength than for the other material.

This in turn means the field required for saturation of the material is much lower; an important consideration due to the limitations of high frequency heating equipment. The final difference in this comparison is that the loop is wider for the higher M_s system, due to a higher coercivity.

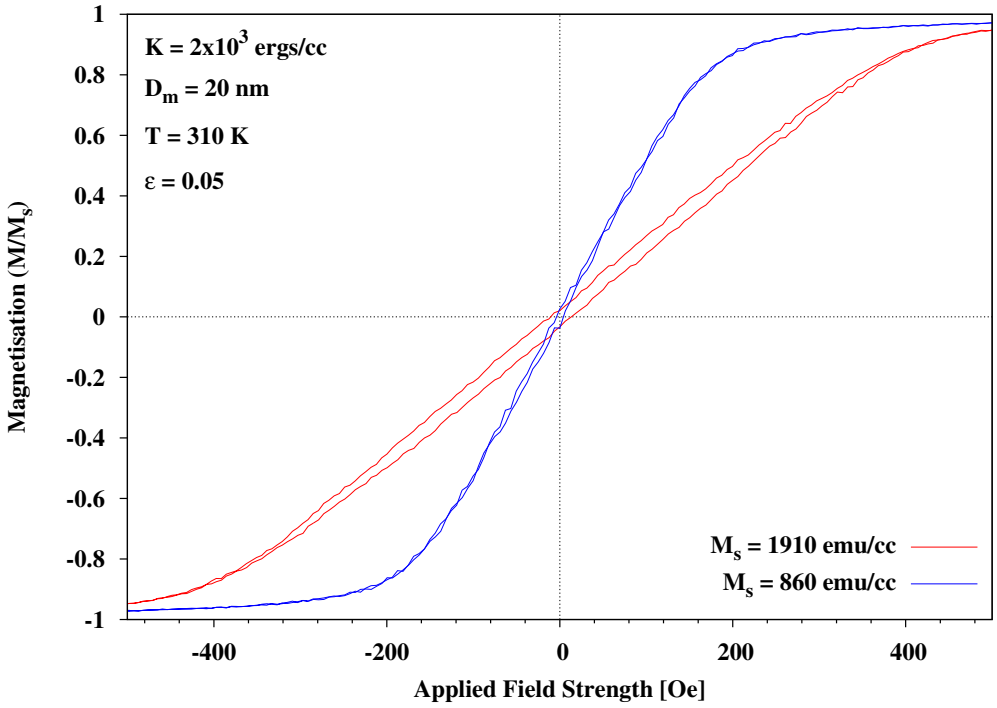

Figure 30: Hysteresis loops for two materials with differing M_s values and constant K. Both systems had median particle diameters of 20 nm and 0.05 packing fraction, frequency of alternating field was 1 kHz.

Remembering that the coercivity is described $H_c \propto 2K/M_s$, this is the opposite trend to that predicted by theory.

Since the particle systems were identical apart from the M_s value, it can be concluded from this simulation that the differences in the shape of the loop are due to an additional effective anisotropy which acts more strongly in the case where M_s is greater. This K_{eff} is due to the dipole-dipole coupling of the interacting particles, which acts to demagnetise the system. At a packing fraction of 0.05 the material simulated here with $M_s = 1910\, emu/cc$ would not saturate in the $100-150\, Oe$ field produced by a heating machine.

5.5 Hysteresis loops: Dependence on K

The anisotropy is a key parameter in determining the coercivity through the relation given below in equation 62, it follows that a larger anisotropy should increase the loop area by increasing the coercivity. In this simulation the M_s value is set and K is varied to observe the effect it has on the shape of the hysteresis loops. The value of saturation magnetisation used was $1710\, emu/cc$, which is the M_s of iron. The anisotropy of iron is $K = 4.2 \times 10^5\, ergs/cc$, and is compared to a system with the anisotropy of magnetite $K = 1 \times 10^5\, ergs/cc$, although the real M_s of magnetite is much

lower than for iron so this result cannot be considered to represent real magnetite.

$$H_c = \frac{2K}{M_s}\left[1 - \left(\frac{ln(tf_0)k_BT}{KV}\right)^{1/2}\right] \tag{62}$$

The K values here are the values for cubic anisotropy of these materials, but in the simulation anisotropy is assumed to be uniaxial as the particles are so small that there will be a large component of shape anisotropy which dominates. The other parameters for these systems were $D_m = 20\,nm$, $\epsilon = 0.05$, $T = 310\,K$, and $f = 1\,kHz$.

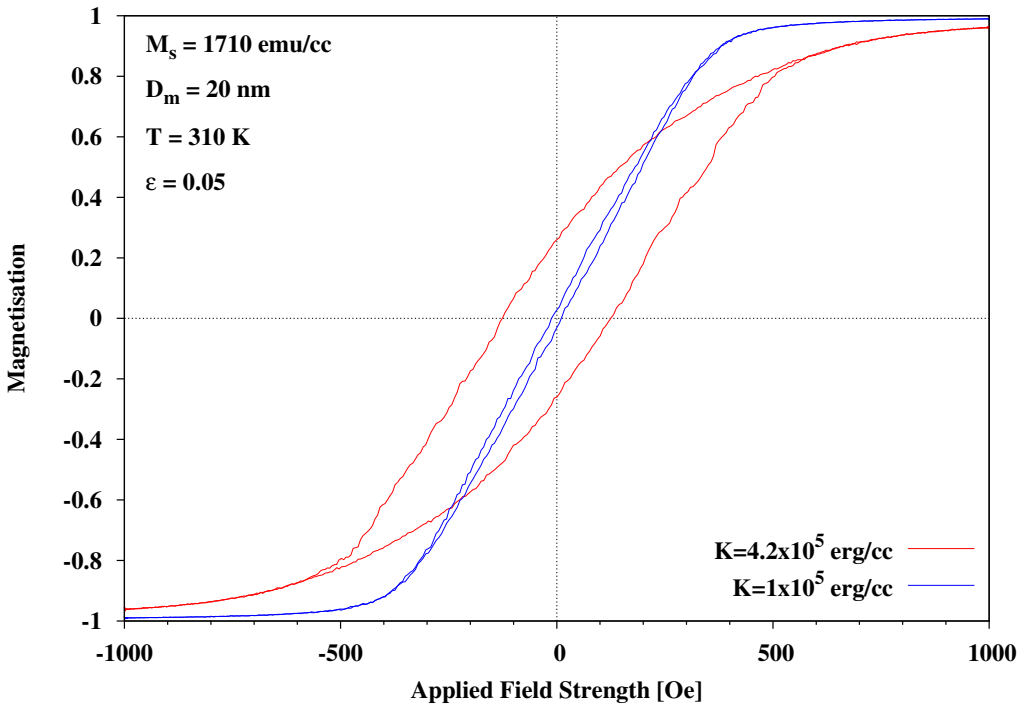

Figure 31: Hysteresis loops for simulations representing iron and magnetite. Both systems had mean particle diameters of $20\,nm$ and 0.05 packing fraction, frequency of alternating field was $1\,kHz$.

The resulting curves are shown in figure 31 and it can be seen that the applied field strength necessary to saturate both materials is much higher than for the materials in figure 30, this is due to the significantly higher intrinsic anisotropies of iron and magnetite. The higher anisotropy also reduces the gradient of the curve. The system of iron particles, having larger K produces a wider hysteresis loop defined by larger values of both H_c and M_r, and has a correspondingly larger area.

5.6 Hysteresis loops: Dependence on field sweep-rate

The hysteresis loops of systems having many particles near the superparamagnetic limit will widen when subjected to a higher frequency ac field or rate. The equation for H_c can be written in both frequency-dependent and rate-dependent form. However, increasing frequency and rate is only

equivalent when the value of H_{max} is constant, due to the relationship $H_{\text{rate}} = 4\, f\, H_{\text{max}}$. In order to discover to which the coercivity is responding an investigation was done whereby manipulation of H_{max} the frequency and rate were varied individually while the other parameter was kept constant.

For this simulation a system of cobalt particles was chosen because cobalt is strongly magnetic and shows a large response in loop width to change in frequency. Hexagonal close packed cobalt has a uniaxial anisotropy constant of $4 \times 10^6\, ergs/cc$ and M_s of $1400\, emu/cc$, and requires a field of at least $\sim\ 4\, kOe$ to saturate it. A field strength of less than this would result in the formation of minor loops and would negate the experiment, consequently the range of H_{max} over which the system was simulated was $4 - 8\, kOe$ in increments of $1\, kOe$. The median particle diameters of the systems which showed the most visible response were 6.5 and $7.5\, nm$, this is because they contain a significant proportion of superparamagnetic particles close to the critical size for the transition to thermally stable behaviour.

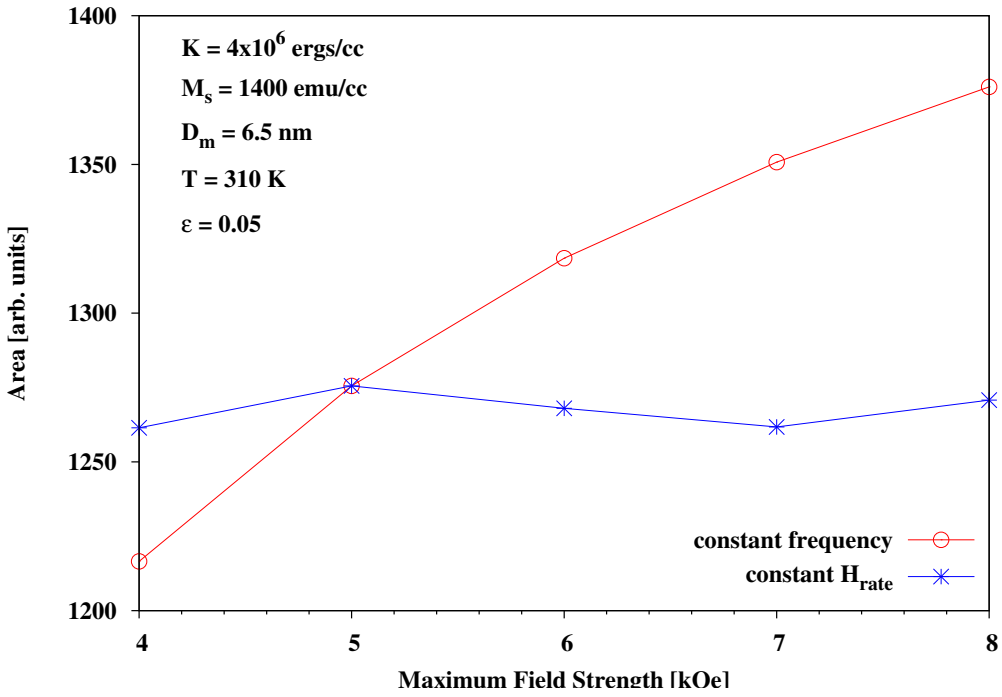

Figure 32: The loop area for a system of cobalt particles when frequency is varied with constant rate (blue line) and when rate is varied with constant frequency for $6.5\, nm$ diameter particles.

As is shown in figure 32, when the maximum field is varied with frequency to maintain a constant rate of $4 \times 10^6\, Oe/s$ the area of the hysteresis loop does not increase. Whereas when rate is varied at a constant frequency of $200\, Hz$ the hysteresis loop area is increased for higher H_{max} where H_{rate} is correspondingly large. The curves for $7.5\, nm$ particles showed the same trend as these $6.5\, nm$ particles. From this it is evident that the coercivity of a system of interacting particles is not dependent on the frequency of the applied field, only on the rate.

5.7 Hysteresis losses: Dependence on frequency

The power loss of the particles through hysteresis is given earlier in equation 58. However, when comparing heat output in systems with different packing fractions, there is more magnetic material in a smaller volume at higher packing fractions automatically increasing the power loss. In order to make a direct comparison of the effectiveness of heating from a range of packing fractions the power is normalised with respect to ϵ.

$$P = \frac{f M_s}{\epsilon} \int M \mathrm{d}H \tag{63}$$

When low frequencies are used the frequency is the dominant factor and the power output is expected to be low since the area of the loop will not be modified significantly by changes in f when f is small. As the frequency applied to systems containing superparamagnetic particles close to the limit for thermally stable behaviour is increased the loop area should also increase, producing a cumulative effect. At very high frequencies the magnetisation of the material cannot respond to the change in field quickly enough to reach saturation resulting in the formation of minor loops. This very quickly reduces the size of the loop area, which becomes the dominant factor and again results in a low power loss. As a consequence of this equation a peak in power loss at an optimum frequency is then expected.

To investigate the peak power loss and find the optimum frequency systems of 1000 particles were initially simulated using 10 frequencies from 10 to $10^{10}\ Hz$ increasing logarithmically at body temperature, $310\,K$. The expression $H_{\text{max}} f < 6.10 \times 10^6$ was used to calculate H_{max} at high frequencies and was capped at $10\,kOe$ for low frequencies, because difficulties in producing the equipment necessary to generate a field so large render it unfeasible for practical applications.

The peak was found for all systems to be located between 10 and $10^6\,Hz$ and so to produce a higher resolution curve the simulations were run for more frequencies within that range. The peaks produced by these simulations contained a lot of noise, particularly towards higher frequencies. This was probably caused by the error in determining the loop area becoming significant as the loop area approached zero. Multiplying this error by the increasingly large frequency produces very jagged curves above $10^5\,Hz$.

To improve the curves a set of results for iron was produced where the hysteresis loop area was found from the average of 20 loops at that frequency and packing fraction. The median diameter was $10\,nm$, and using equations 29 and 60 as before the critical diameter for iron was found to decrease from $11.1\,nm$ to $10.0\,nm$ over the frequency range used. Other parameters were the magnetic saturation of iron $1700\,emu/cc$, and the anisotropy value used was $1 \times 10^6\,ergs/cc$ to account for the expected shape anisotropy in particles with 10% elongation.

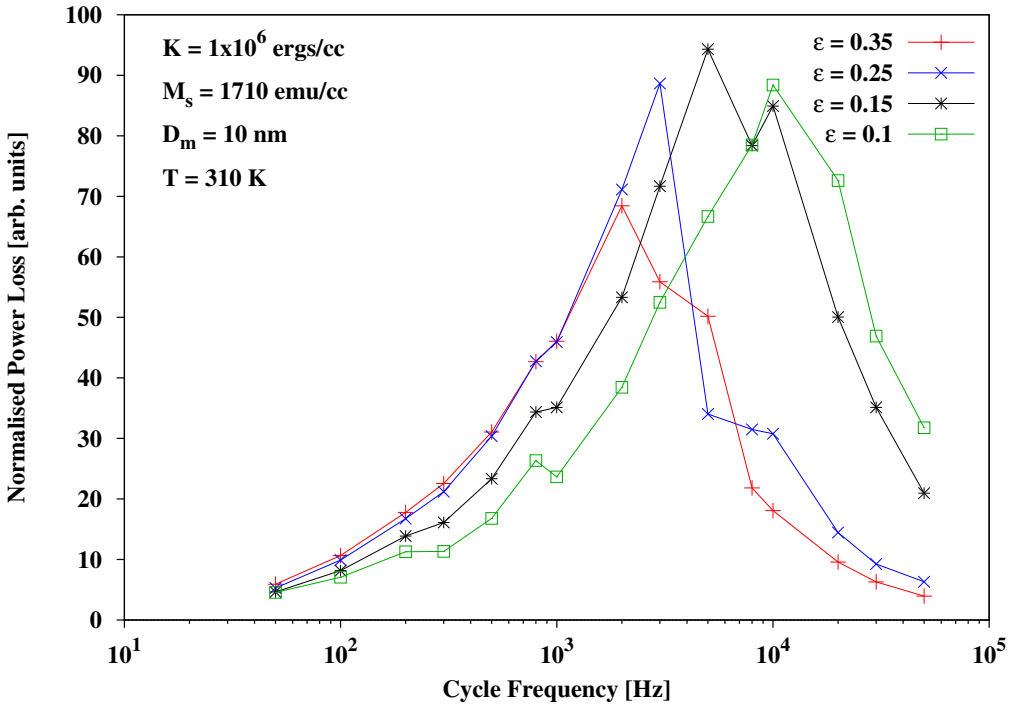

Figure 33: Power loss as a function of frequency, each point calculated from the average area of 20 hysteresis loops.

For clarity only four curves are shown in figure 33. These curves are normalised by the packing fraction; the absolute power loss per unit volume will increase with packing fraction as there will be more magnetic material within the same volume. The curve for the system of 0.05 packing fraction did not have a discernible peak with a power loss roughly constant around 5, indicating that the system remained predominantly superparamagnetic at all frequencies.

The frequency of peak power loss varies with packing fraction and ranges from approximately $2\,kHz$ to $10k\,kHz$. The field strengths at these frequencies decrease from $\sim 3\,kOe$ to $\sim 600\,Oe$. The frequency of the peak power loss is largest for the lowest concentration of particles that respond to the change in frequency, the 0.1 packing fraction system. As the concentration is increased the frequency of the peak is reduced, and for the highest packing fractions where the system is in a non-colloidal state the amplitude of the peak is also reduced.

The same simulation was run for comparison with 3 other systems; $7.5\,nm$ median diameter iron particles, $10\,nm$ median diameter magnetite particles, and $10\,nm$ median diameter iron-platinum particles. The M_s of magnetite is $470\,emu/cc$ and the anisotropy used was $5 \times 10^5\,ergs/cc$ [61] to account for the uniaxial shape anisotropy of small particles with 10% elongation. The M_s of iron-platinum is $1000\,emu/cc$ and the anisotropy used was $5 \times 10^6\,ergs/cc$. Due to limitations in computational time it was not possible to generate the results for these systems over an average of 20 hysteresis loops, consequently the curves for all concentrations were affected by some degree of noise which reduced the accuracy with which the frequency of the peak could be estimated.

The data was particularly unreliable for systems where the power loss values were low, these included many of the lowest concentrations as well as all the data for magnetite. This is because the critical diameter for magnetite over the frequency range of this simulation was $12.6 - 14.0\,nm$, so most of the particles in the magnetite systems would have remained superparamagnetic for all frequencies and no power loss peak would form.

The systems of $7.5\,nm$ iron particles gave overall lower power outputs than the $10\,nm$ systems, the largest value of the power loss was 40 compared to values of ~ 90 for the larger particles. This is because a larger fraction of the particles with smaller median diameter will have remained superparamagnetic for all frequencies. The lowest 3 packing fractions showed no clear peak at all and this data has not been included in the final comparison.

The iron-platinum particles in these conditions have a critical diameter range of $5.8 - 6.5\,nm$ and so for a system with a median diameter of $10\,nm$ the majority of the particles should be thermally stable. However, the largest power loss outputs for the FePt systems were lower than for the $7.5\,nm$ iron systems, it is likely that the anisotropy of iron-platinum being 5 times larger than that of iron lead to the formation of minor loops for many of the mid to high frequencies, where H_{max} was reduced in accordance with the expression $H_{max}f < 6 \times 10^6\,Oe/s$. For these systems only the three highest packing fractions formed clear peaks.

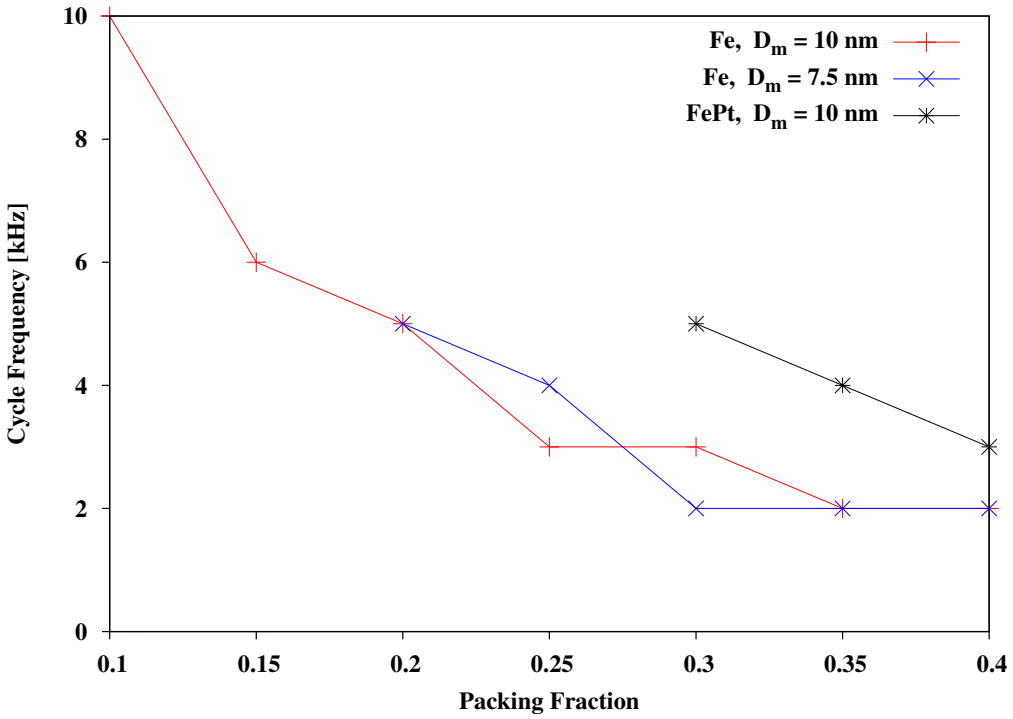

Figure 34: The frequency at which hysteresis losses peak plotted against the packing fraction for three systems: $10\,nm$ Fe, $7.5\,nm$ Fe, and $10\,nm$ FePt.

The frequencies of the power loss peak for all systems that could be determined are compiled in figure 34. As can be seen the frequency of the peak decreases steadily as the packing fraction increases, although it appears to reach a minimum at $2\,kHz$ for both systems of iron.

5.8 Summary

For known concentrations of iron particles the optimum frequency for producing the most hysteresis heating can be found. When the median diameter of the particles in the system is close to the critical diameter for the transition to superparamagnetic behaviour the reduction in critical diameter as frequency increases expands the hysteresis loop area, which together work to increase the amount of heat produced by hysteresis.

The frequency of peak power loss is very similar for the particle system with median diameter $7.5\,nm$, however the magnitude of the power loss was substantially less as many particles did not contribute to the hysteresis heating as they were smaller than the critical size. The most heat can be generated when the median diameter of the system is approximately equal to or just larger than the critical size.

The effect of the packing fraction on the power loss is not straightforward. At high frequencies using lower packing fractions increases heating effect compared to close packed systems. However, at low frequencies using higher packing fractions increases amount of heating. And in the region where the frequencies of peak power loss are located there is crossover of these two trends as the higher packing fractions reach their peak first and the heating effect begins to drop off rapidly.

In addition, for the highest packing fractions the amplitude of the peak is noticably reduced, which lowers the maximum heat output that can be obtained from these systems. Considering that the peaks for colloidal states are of approximately the same magnitude, and that a higher frequency cycles the hysteresis loop more often in the same amount of time, the largest heat output for iron in these simulations is achieved using a packing fraction of 0.1. At this frequency the maximum field strength required is only $\sim\ 600\,Oe$, which as the lowest maximum field strength is closest to the values that are currently produced by clinical treatment machines, and therefore the most realistic set of parameters for practical application.

The results of this simulation indicate that particles of iron-platinum are perhaps not suitable for hyperthermia as only the highest packing fractions, which are representative of non-colloidal states, produce a significant powerloss. In vivo it will be difficult to ensure that such high concentrations are reached uniformly over the treatment area, and it must be remembered that there are limits to the volume of magnetic material that can be safely injected into human patients.

The results for magnetite in this case are not illuminating. The simulation was run for systems of magnetite particles that were too small to generate a large amount of heat via hysteresis. To generate some data that can be used to find the optimum frequency the median diameter used should be closer to $15\,nm$, so that a larger fraction of the particles are thermally stable. Also further work with this simulation could take into account that systems of real particles usually have a larger size distribution which would increase the number of blocked particles for the same median diameter.

Appendix

Software

```
//Shrinking algorithm for generating random systems of a given packing density
//Author: F C Burrows
//Last modified: 2 Mar 2011

#include<iostream>
#include<fstream>
#include<cstdlib>
#include<string>
#include<sstream>
#include<iomanip>
#include<vector>
#include<algorithm>
#include<cmath>
#include<cassert>
#include<time.h>
#include"../Tom/CONFIG.h"
#include"../Tom/TOOLS.h"
#include"../Joe/array3d.h"
#include"../RNGs/stocc.h"
#include"../RNGs/stoc1.cpp"
#include"../RNGs/mersenne.cpp"
#include"../RNGs/userintf.cpp"

//======================initialise random number generator=====================
namespace nsrandom{ CRandomMersenne RanGen(12345); }

//======================define arrays for particle positions====================
namespace particles{
std::vector<double> rad_array(0);
std::vector<double> vol_array(0);
std::vector<double> px_array(0);
std::vector<double> py_array(0);
std::vector<double> pz_array(0);
Array3D< std::vector<int> > cell_array; }

//================================SUBROUTINE=====================================
//==============================initialise arrays================================
double init(const int n, const double dm, const double s, double& v){

particles::rad_array.resize(n,0.0);
particles::vol_array.resize(n,0.0);
particles::px_array.resize(n,0.0);
particles::py_array.resize(n,0.0);
particles::pz_array.resize(n,0.0);

//=================generate a lognormal distribution of radii================
double var;
double box_size = 4.0*double(pow(n,1./3.))*dm;
std::cout<<"box size set to "<< box_size << " Angstroms" <<std::endl;

for(int i=0; i<n; i++){

  double R, R1, R2;
  for(;;){
    R1 = 2.0*nsrandom::RanGen.Random()-1.0;
    R2 = 2.0*nsrandom::RanGen.Random()-1.0;
    R = R1*R1 + R2*R2;
  if(R<1.0) break; }
```

```
  var = R1*sqrt(-2.0*log(R)/R);
  particles::rad_array[i] = 0.5*exp(var*s)*dm;

//=========================calculate particle volumes=========================
  particles::vol_array[i] = (4./3.)*M_PI*particles::rad_array[i]
                          * particles::rad_array[i]*particles::rad_array[i];
  v += particles::vol_array[i];

//================generate random positions for the particles================
  particles::px_array[i] = nsrandom::RanGen.Random()*box_size;
  particles::py_array[i] = nsrandom::RanGen.Random()*box_size;
  particles::pz_array[i] = nsrandom::RanGen.Random()*box_size; }
return box_size; }

//================================SUBROUTINE==================================
//=========================create neighbour list==============================
int neighbourlist(int n, const double box_size, const double range){

int num_cells = int(box_size/(1.1*range));
double cell_size = box_size/double(num_cells);

std::cout<< "cell size: " << cell_size <<std::endl;
std::cout<< "number of cells: " << num_cells << " cubed" <<std::endl;

//==================allocating the 3D vector array dimensions================
particles::cell_array.resize(num_cells,num_cells,num_cells);

for(int x=0; x<num_cells; ++x) {
  for(int y=0; y<num_cells; ++y) {
    for(int z=0; z<num_cells; ++z) {
      particles::cell_array(x,y,z).clear();
      particles::cell_array(x,y,z)
                .reserve(int(n/(num_cells*num_cells*num_cells)));
}}}

//====================allocating the particles to their cells================
for(int i=0; i<n; i++){

  int x = int(particles::px_array[i]/cell_size);
  int y = int(particles::py_array[i]/cell_size);
  int z = int(particles::pz_array[i]/cell_size);
  particles::cell_array(x,y,z).push_back(i); }

//==============checking that all particles have been allocated===============
int count = 0;
for(int x=0; x<num_cells; x++){
  for(int y=0; y<num_cells; y++){
    for(int z=0; z<num_cells; z++){

      count = count + particles::cell_array(x,y,z).size();
}}}

if(count != n){
  std::cout<<"\nERROR (Particles unaccounted for)\nEXITING\n"<<std::endl;
  exit(1); }
return num_cells; }

//================================SUBROUTINE==================================
//==================check for overlaps and expand system======================
double expand(const int n, double box_size, const int num_cells){

int count=0, cellx, celly, cellz;
double factor = 0;

for(int x=0; x<num_cells; x++){
```

```
  for(int y=0; y<num_cells; y++){
    for(int z=0; z<num_cells; z++){

  for(unsigned int a=0; a<particles::cell_array(x,y,z).size(); a++){

    int i = particles::cell_array(x,y,z).at(a);
    double wrapx, wrapy, wrapz;

    for(int xcount=(x-1); xcount<(x+2); xcount++){
      if(xcount>num_cells-1){ cellx = 0; wrapx = box_size;}
      else if(xcount<0){ cellx = num_cells-1; wrapx = -box_size;}
      else{ cellx = xcount; wrapx = 0;}

      for(int ycount=(y-1); ycount<(y+2); ycount++){
       if(ycount>num_cells-1){ celly = 0; wrapy = box_size;}
        else if(ycount<0){ celly = num_cells-1; wrapy = -box_size;}
        else{ celly = ycount; wrapy = 0;}

        for(int zcount=(z-1); zcount<(z+2); zcount++){
          if(zcount>num_cells-1){ cellz = 0; wrapz = box_size;}
          else if(zcount<0){ cellz = num_cells-1; wrapz = -box_size;}
          else{ cellz = zcount; wrapz = 0;}

          for(unsigned int
              b=0; b<particles::cell_array(cellx,celly,cellz).size(); b++){

            int j = particles::cell_array(cellx,celly,cellz).at(b);
            if(i==j) continue;

//=====separation between centerpoints calculated using vector subtraction=====
            double dpx = fabs(particles::px_array[i]
                        - (particles::px_array[j]+wrapx));
            double dpy = fabs(particles::py_array[i]
                        - (particles::py_array[j]+wrapy));
            double dpz = fabs(particles::pz_array[i]
                        - (particles::pz_array[j]+wrapz));

            double separation = sqrt(dpx*dpx+dpy*dpy+dpz*dpz);

//=============if statement is true the system will need expanding=============
            if(separation < particles::rad_array[i]+particles::rad_array[j]){
              count += 1;
              double expnd = (particles::rad_array[i]+particles::rad_array[j])
                           / separation;

//=========================find largest value of expand==========================
              if(expnd > factor) factor = expnd;
  }}}}}}
}}}

//================================expand the system================================
if(count != 0){

  factor *= 1.01;
  box_size *= factor;

  for(int i=0; i<n; i++){

    particles::px_array[i] *= factor;
    particles::py_array[i] *= factor;
    particles::pz_array[i] *= factor; }}
return box_size; }

//================================SUBROUTINE================================
//=========================check for overlaps again=========================
```

```
int overlap(const int num_cells, const double box_size){

int count = 0, cellx, celly, cellz;
double ovrlap = 0;
for(int x=0; x<num_cells; x++){
  for(int y=0; y<num_cells; y++){
    for(int z=0; z<num_cells; z++){

  for(unsigned int a=0; a<particles::cell_array(x,y,z).size(); a++){

    int i = particles::cell_array(x,y,z).at(a);
    double wrapx, wrapy, wrapz;

    for(int xcount=(x-1); xcount<(x+2); xcount++){
      if(xcount>num_cells-1){ cellx = 0; wrapx = box_size;}
      else if(xcount<0){ cellx = num_cells-1; wrapx = -box_size;}
      else{ cellx = xcount; wrapx = 0;}

      for(int ycount=(y-1); ycount<(y+2); ycount++){
       if(ycount>num_cells-1){ celly = 0; wrapy = box_size;}
        else if(ycount<0){ celly = num_cells-1; wrapy = -box_size;}
        else{ celly = ycount; wrapy = 0;}

        for(int zcount=(z-1); zcount<(z+2); zcount++){
          if(zcount>num_cells-1){ cellz = 0; wrapz = box_size;}
          else if(zcount<0){ cellz = num_cells-1; wrapz = -box_size;}
          else{ cellz = zcount; wrapz = 0;}

          for(unsigned int
              b=0; b<particles::cell_array(cellx,celly,cellz).size(); b++){

            int j = particles::cell_array(cellx,celly,cellz).at(b);
            if(i==j) continue;

            double dpx = fabs(particles::px_array[i]
                        - (particles::px_array[j]+wrapx));
            double dpy = fabs(particles::py_array[i]
                        - (particles::py_array[j]+wrapy));
            double dpz = fabs(particles::pz_array[i]
                        - (particles::pz_array[j]+wrapz));

            double separation = sqrt(dpx*dpx+dpy*dpy+dpz*dpz);
            if(separation < (particles::rad_array[i]+particles::rad_array[j])){
              count += 1;
              double check = particles::rad_array[i]
                           + particles::rad_array[j]-separation;
              if(check > ovrlap) ovrlap=check;
  }}}}}}
}}}
if(count!=0){
std::cout<<"\nERROR (Particles overlapping after shrink)"<<std::endl;
exit(1); }
return 0; }

//================================SUBROUTINE=====================================
//============================do monte carlo moves================================
double montecarlo(const int n, const double dm, const double box_size,
                  const int num_cells, const int M, double& delta){

const double cell_size = box_size/double(num_cells);
int temp [n];

for(int m=0; m<M; m++){

//======================random order for each iteration=======================
```

```
      int seed = nsrandom::RanGen.Random()*100000;
      StochasticLib1 sto(seed);
      sto.Shuffle(temp, 0, n);

      int Acount = 0, Rcount = 0, ovrlap=0, cellchanges=0;
      int index, cellx, celly, cellz;
261   for(int b=0; b<n; b++){

        int i = temp[b];

    //=======================reinitialise for each particle=======================
        bool reject = false, accept = false;
        double E = 0.0, Enew = 0.0;

    //===========================generate new position============================
        double x = particles::px_array[i];
271     double y = particles::py_array[i];
        double z = particles::pz_array[i];

        double newx = x + delta*(nsrandom::RanGen.Random()*2.-1.);
        double newy = y + delta*(nsrandom::RanGen.Random()*2.-1.);
        double newz = z + delta*(nsrandom::RanGen.Random()*2.-1.);

    //=========================periodic boundary conditions=======================
        if(newx>=box_size) newx = newx - box_size;
        if(newx<0) newx = newx + box_size;
281     if(newy>=box_size) newy = newy - box_size;
        if(newy<0) newy= newy + box_size;
        if(newz>=box_size) newz = newz - box_size;
        if(newz<0) newz = newz + box_size;

    //================check to see if the particle has moved cells================
        int cx = int(x/cell_size);
        int cy = int(y/cell_size);
        int cz = int(z/cell_size);

291     int ncx = int(newx/cell_size);
        int ncy = int(newy/cell_size);
        int ncz = int(newz/cell_size);

    //============if so, find the index it is stored under in cell_array==========
        if(cx!=ncx||cy!=ncy||cz!=ncz){

          std::vector<int>::const_iterator lookfor =
                            particles::cell_array(cx,cy,cz).begin();
          lookfor = std::find(particles::cell_array(cx,cy,cz).begin(),
301                           particles::cell_array(cx,cy,cz).end(),i);
          assert(lookfor != particles::cell_array(cx,cy,cz).end() );
          index = lookfor - particles::cell_array(cx,cy,cz).begin(); }

    //====================loop over particles in surrounding cells=================
        double wrapx, wrapy, wrapz;

        for(int xcount=ncx-1; xcount<ncx+2; xcount++){
          if(xcount>num_cells-1){ cellx = 0; wrapx = box_size;}
          else if(xcount<0){ cellx = num_cells-1; wrapx = -box_size;}
311       else{ cellx = xcount; wrapx = 0;}

          for(int ycount=ncy-1; ycount<ncy+2; ycount++){
            if(ycount>num_cells-1){ celly = 0; wrapy = box_size;}
            else if(ycount<0){ celly = num_cells-1; wrapy = -box_size;}
            else{ celly = ycount; wrapy = 0;}

            for(int zcount=ncz-1; zcount<ncz+2; zcount++){
              if(zcount>num_cells-1){ cellz = 0; wrapz = box_size;}
```

```
            else if(zcount<0){ cellz = num_cells-1; wrapz = -box_size;}
            else{ cellz = zcount; wrapz = 0;}

            for(unsigned int
                a=0; a<particles::cell_array(cellx,celly,cellz).size(); a++){

              int j = particles::cell_array(cellx,celly,cellz)[a];

              if(i==j) continue;

              double xj = particles::px_array[j]+wrapx;
              double yj = particles::py_array[j]+wrapy;
              double zj = particles::pz_array[j]+wrapz;

              double newsepn = sqrt(fabs(newx-xj)*fabs(newx-xj)
                                  + fabs(newy-yj)*fabs(newy-yj)
                                  + fabs(newz-zj)*fabs(newz-zj));

    //==================if overlap, reject and break from loops==================
              double radsum = particles::rad_array[i] + particles::rad_array[j];
              if(newsepn < radsum){ reject = true; ovrlap +=1; break; }

    //===========calculate contribution of j to energy of particle i===============
              double oldsepn = sqrt(fabs(x-xj)*fabs(x-xj)
                                  + fabs(y-yj)*fabs(y-yj)
                                  + fabs(z-zj)*fabs(z-zj));
              double olddist = oldsepn - radsum;
              double newdist = newsepn - radsum;

              E += 1.e-4*(dm/olddist)*(dm/olddist)*(dm/olddist)*(dm/olddist);
              Enew += 1.e-4*(dm/newdist)*(dm/newdist)*(dm/newdist)*(dm/newdist);
                  }

            if(reject == true) break; }
          if(reject == true) break; }
        if(reject == true) break; }
      if(reject != true){

    //=================if Monte Carlo criteria not met --> reject=================
      double deltaE = Enew - E;

      if(deltaE < 0) accept = true;
      else if(exp(-deltaE) < nsrandom::RanGen.Random()) accept = true;
      else { reject = true; Rcount++ ; continue; }

    //======================store coordinates of new position=====================
      particles::px_array[i] = newx;
      particles::py_array[i] = newy;
      particles::pz_array[i] = newz;

    //================if particle moved cells, update neighbour list==============
      if(cx!=ncx||cy!=ncy||cz!=ncz){
        particles::cell_array(cx,cy,cz)
                  .erase(particles::cell_array(cx,cy,cz).begin()+index);
        particles::cell_array(ncx,ncy,ncz).push_back(i);
        cellchanges += 1; }

      Acount++;
      if(reject == accept){
        std::cout<<"\nERROR (bool accept == bool reject) EXITING\n"<<std::endl;
        exit(1); } }
    else Rcount++; }

    if(Acount+Rcount != n){
      std::cout<<"\nERROR (Particles unaccounted for) EXITING\n"<<std::endl;
```

```
    exit(1); }

//=========================tuning to ~50% rejection rate=========================
  double tuner = double(Rcount)/double(n);
  delta = delta*(0.5/tuner);

  if(delta > 0.5*dm){ delta = 0.5*dm;}      //max delta
  if(delta < 0.1*dm){ delta = 0.1*dm;}  }   //min delta
return 1; }

//================================SUBROUTINE=====================================
//============================deterministic shrink================================
double shrink(const int n, double box_size, const int num_cells,
              const double vol, const double pkf, bool& finalshrink){

int cellx, celly, cellz;
double factor = 0.;

for(int x=0; x<num_cells; x++){
  for(int y=0; y<num_cells; y++){
    for(int z=0; z<num_cells; z++){

  for(unsigned int a=0; a<particles::cell_array(x,y,z).size(); a++){

    int i = particles::cell_array(x,y,z).at(a);
    double wrapx, wrapy, wrapz;

    for(int xcount=(x-1); xcount<(x+2); xcount++){
      if(xcount>num_cells-1){ cellx = 0; wrapx = box_size;}
      else if(xcount<0){ cellx = num_cells-1; wrapx = -box_size;}
      else{ cellx = xcount; wrapx = 0;}

      for(int ycount=(y-1); ycount<(y+2); ycount++){
       if(ycount>num_cells-1){ celly = 0; wrapy = box_size;}
        else if(ycount<0){ celly = num_cells-1; wrapy = -box_size;}
        else{ celly = ycount; wrapy = 0;}

        for(int zcount=(z-1); zcount<(z+2); zcount++){
          if(zcount>num_cells-1){ cellz = 0; wrapz = box_size;}
          else if(zcount<0){ cellz = num_cells-1; wrapz = -box_size;}
          else{ cellz = zcount; wrapz = 0;}

          for(unsigned int
              b=0; b<particles::cell_array(cellx,celly,cellz).size(); b++){

            int j = particles::cell_array(cellx,celly,cellz).at(b);
            if(i==j) continue;

            double dpx = fabs(particles::px_array[i]
                       - (particles::px_array[j]+wrapx));
            double dpy = fabs(particles::py_array[i]
                       - (particles::py_array[j]+wrapy));
            double dpz = fabs(particles::pz_array[i]
                       - (particles::pz_array[j]+wrapz));

            double separation = sqrt(dpx*dpx+dpy*dpy+dpz*dpz);

            double shrnk = (particles::rad_array[i]+particles::rad_array[j])
                         / separation;

            assert(shrnk < 1.);
            if(shrnk > factor) factor = shrnk;
  }}}}}
}}}
```

```
    factor = 1.0001*factor;

451 if(factor>1.0 or factor==1.0) {
    return box_size;}

    //==================test so that system doesn't shrink too much================

    double testboxsize = box_size*factor;
    double testvol = testboxsize*testboxsize*testboxsize;
    double testpkf = (vol/testvol);
    if(testpkf>pkf){
      std::cout<<"FINAL SHRINK"<<std::endl;
461   finalshrink = 1;
      testvol = (vol/pkf);
      testboxsize = pow(testvol,(1./3.));
      factor = testboxsize/box_size; }

    box_size *=factor;
    for(int i=0; i<n; i++){

      particles::px_array[i] *= factor;
      particles::py_array[i] *= factor;
471   particles::pz_array[i] *= factor; }
    return box_size; }

    //================================SUBROUTINE=====================================
    //=========================outputting data to file================================
    int output(const int n, const double m, const double s, const double pkf,
               const double bs){

    std::stringstream outfile_sstr;
    outfile_sstr << "config";
481 outfile_sstr << std::setfill('0') << std::setw(2);
    outfile_sstr << pkf*100 << ".dat";
    std::string outfile = outfile_sstr.str();

    FILE * pFile;
    pFile = fopen(outfile.c_str(),"w");

    fprintf(pFile,"%f\t\t%f\t\t%d\t\t%f\n",bs,m,n,pkf);

    for(int i=0; i<n; i++){
491
      fprintf(pFile,"%12.6f\t\t%12.6f\t\t%12.6f\t\t%7.6f\n",
              particles::px_array[i],particles::py_array[i],
              particles::pz_array[i],2.0*(particles::rad_array[i]/double(m))); }
    fclose(pFile);
    return 1; }

    //================================================================================
    //================================================================================

501 int main(int argc,char *argv[]){

    int num_particles, mc_moves;
    double median_diameter, sigmaD, packing_fraction, volume=0.0;
    bool finalshrink = 0;

    //=============check that when ran executable included input file==============
    if(argc < 2){
      std::cerr << "You must give a setup file" << std::endl;
      exit(0); }
511
    //=========================open and read the config file=======================
    std::string cfgfile = std::string(argv[1]);
```

```
    Config cfg(cfgfile);
    std::cout << "\n\nSetup file is " << cfgfile << std::endl;

    num_particles = cfg.read<int>("num_particles");
    num_particles = num_particles*num_particles*num_particles;
    median_diameter = cfg.read<double>("median_diameter");
    sigmaD = cfg.read<double>("sigmaD");
521 packing_fraction = cfg.read<double>("packing_fraction");
    mc_moves = cfg.read<int>("mc_moves");

    //=========================use inputs to initialise arrays=======================
    double box_size = init(num_particles, median_diameter, sigmaD, volume);

    //===============create a list of which cell each particle is in===============
    double range = 4**max_element(particles::rad_array.begin(),
                                  particles::rad_array.end());
    int num_cells = neighbourlist(num_particles, box_size, range);
531
    //=======================expand system to remove overlaps=======================
    box_size = expand(num_particles, box_size, num_cells);

    overlap(num_cells, box_size);

    //==========================regenerate neighbour list============================
    num_cells = neighbourlist(num_particles, box_size, range);

    //===========================check current percentage============================
541 double Tvol = box_size*box_size*box_size;
    double Pvol = (volume/Tvol);
    double delta = 0.5*median_diameter;             //original value for delta

    while(Pvol<packing_fraction){

    //=======================monte carlo moves on particles=========================
      montecarlo(num_particles, median_diameter, box_size, num_cells, mc_moves,
                 delta);

551 //==============================shrink the system================================
      box_size = shrink(num_particles, box_size, num_cells, volume,
                        packing_fraction, finalshrink);

      overlap(num_cells, box_size);
    //=======================check percentage after shrink==========================
      Tvol = box_size*box_size*box_size;
      Pvol = (volume/Tvol);

    //==========================regenerate neighbour list============================
561   num_cells = neighbourlist(num_particles, box_size, range);

      if(finalshrink==1) break; }

    //=======================monte carlo moves on particles=========================
      montecarlo(num_particles, median_diameter, box_size, num_cells, mc_moves,
                 delta);

    //============================output data to file================================
      output(num_particles, median_diameter, sigmaD, packing_fraction, box_size);
571 return 0; }
```

List of symbols

A

a	one of three equivalent axis in a cubic crystal or the minor axis in a particle
α	angle between applied field and the easy axis
$\alpha_{1,2,3}$	cosine of the angle between direction of magnetisation and crystal axes a, b, c

B

b	one of three equivalent axis in a cubic crystal

C

c	one of three equivalent axis in a cubic crystal or the major axis in a particle
χ	susceptibility
χ'	real component of susceptibility
χ''	imaginary component of susceptibility
χ_0	equilibrium susceptibility

D

D_c	critical diameter
D_m	median diameter
D_S	Shliomis diameter

E

E	energy
E_H	energy produced by hysteresis
E_i	energy of a particle i
E_{max}	maximum energy for moment in a particle
E_{min}	minimum energy for moment in a particle
E_{cubic}	anisotropy energy for a cubic grain or particle
E_{uniaxial}	anisotropy energy for a uniaxial grain or particle
E_0	energy at the peak of the energy barrier
E_+	energy of the minimum parallel to the easy axis
E_-	energy of the minimum antiparallel to the easy axis
ΔE	energy barrier or change in energy
ΔE_i	change in energy of particle i in a Monte-Carlo move
ΔE_c	critical energy barrier
ΔE_{eff}	effective energy barrier due to dipolar interactions
ϵ	packing density
η	viscosity of a fluid

F

f	frequency
f_0	attempt frequency
ϕ	polar co-ordinate describing the moment of a particle relative to the easy axis

G

γ	energy density of a domain wall

H

h	reduced field
h_c	reduced coercivity
H	magnetic field
H_{app}	applied field
H_c	coercive field
H_K	anisotropy field
H_K^{eff}	effective anisotropy field due to dipolar interactions
H_{loc}	local field, effective field at a point
H_t	threshold field, where energy barrier and energy minimum are equal
H_{max}	local field, effective field at a point
H_{rate}	local field, effective field at a point
ΔH	Step change in Magnetic Field

K

k_B	Boltzmann constant ($1.38 \times 10^{-16}\, ergs/cc$)
K	anisotropy constant
K_0	anisotropy constant (independent of angle)
K_1	first anisotropy constant
K_2	second anisotropy constant
K_c	anisotropy constant due to crystalline effects
K_{eff}	effective anisotropy due to interaction effects
K_s	anisotropy constant due to shape effects
K_u	uniaxial anisotropy constant

L

$L(\zeta)$	Langevin function

M

m	normalised magnetisation
M	magnetisation
M_r	remanence magnetisation
M_r^{max}	maximum remanence magnetisation
M_s	saturation magnetisation
μ	a single magnetic moment
μ_0	permeability of free space ($4\pi \times 10^{-7}\, kg\, m/A^2 s^2$)

N

n	number of points on the curve
N	number of particles in the system
N_c	demagnetising factor along the c-axis of an elongated particle
N_a	demagnetising factor along the a-axis of an elongated particle
N_{mcs}	number of Monte-Carlo moves

P

P	power
P_i	probability of magnetic reversal for particle i
P_+	probability of moment to be parallel to the easy axis
P_-	probability of moment to be antiparallel to the easy axis
ψ	angle between the anisotropy direction and the applied field

R

r_{ij}	distance between the centre points of two particles i and j
r_c	critical radius for transition between single domain and multi-domain particle
r_h	hydrodynamic radius of particles in a fluid
r_{max}	maximum range for contributions to interactions from particles j
R	rate of change of field / sweep-rate
R_0	initial rate of change of field

S

S	rate of logarithmic decay of the magnetisation
σ	standard deviation of the lognormal distributions

T

t	time
t_m	measurement time
t_{eff}	effective time for translating between stepped and swept field process
δt	time interval equal to the number of Monte-Carlo moves times one timestep
Δt	timestep
T	temperature
T_B	temperature for transition between superparamagnetic and stable behaviour
T_C	Curie temperature
θ	angle between direction of magnetisation or moment and the easy axis
τ_{eff}	effective relaxation time
τ_B	Brownian relaxation time
τ_N	Neel relaxation time

V

V	volume of a particle
V_c	critical volume for transition between superparamagnetic and stable behaviour
V_m	median volume of the particles in the system

W

w_+	transition rate of moment from parallel to antiparallel relative to the easy axis
w_-	transition rate of moment from antiparallel to parallel relative to the easy axis
ω	angular frequency

Z

Z	partition function of the Boltzmann distribution

References

[1] J. L. Phillips. A topical review of magnetic fluid hyperthermia. *Presented at the American Institute of Chemical Engineers Conference*, 2005.

[2] D-H. Kim, K-N. Kim, K-M. Kim, I-B Shim, and Y-K. Lee. Necrosis of carcinoma cells using $Co_{1-x}Ni_xFe_2O_4$ and $Ba_{1-x}Sr_xFe_{12}O_{19}$ ferrites under alternating magnetic field. *IEEE Trans. Magn.*, 40:2985–2987, 2004.

[3] B. Hildebrandt, P. Wust, O. Ahlers, A. Dieing, G. Sreenivasa, T. Kerner, R. Felix, and H. Riess. The cellular and molecuar basis of hyperthermia. *Crit. Rev. Oncol. Hematol.*, 43:33–56, 2002.

[4] S. P. Tomasovic. Biological basis for hyperthermia in cancer treatment. *Presented at the IEEE Engineering in Medicine and Biology Society 10th annual international conference*, 1988.

[5] K. Maier-Hauff, F. Ulrich, D. Nestler, H. Niehoff, P. Wust, B. Thiesen, H. Orawa, V. Budach, and A. Jordan. Efficacy and saftey of intratumoral thermotherapy using magnetic iron-oxide nanoparticles combined with external beam radiotherapy on patients with recurrent giloblastoma multiforme. *Int. J. Neurooncol.*, pages 317–241, 2011.

[6] C. W. Song, H. J. Park, C. K. Lee, and R. Griffin. Implications of increased tumor blood flow and oxygenation caused by mild temperature hyperthermia in tumor treatment. *International Journal of Hyperthermia*, 41:761–767, 2005.

[7] J. van der Zee. Heating the patient: a promising approach? *Annals of Oncology*, 13:1173–1184, 2002.

[8] G. M. Hahn. Potential for therapy of drugs and hyperthermia. *Cancer Research*, 39:2264–2268, 1979.

[9] K. Abe, N. Shiozawa, and M. Makikawa. Hyperthermia system with thermoseed set in abdominal cavity and ac-magnetic field. *Presented at the IEEE Engineering in Medicine and Biology Society 29th Annual Conference*, 2007.

[10] A. Jordan, R. Scholz, K. Maier-Hauff, M. Johannsen, P. Wust, J. Nadobny, H. Schirra, H. Schmidt, S. Deger, S. Loening, W. Lanksch, and R. Felix. Presentation of a new magnetic field therapy system for the treatment of human solid tumors with magnetic fluid hyperthermia. *J. Magn. Magn. Mater.*, 225:118–126, 2001.

[11] A. Jordan, R. Scholz, K. Maier-Hauff, F. K. H. van Landeghem, N. Waldoefner, U. Teichgraeber, J. Pinkernell, H. Bruhn, F. Neumann, B. Thiesen, A. von Deimling, and R. Felix. The effect of thermotherapy using magnetic nanoparticles on malignent rat glimoa. *Int. J. Neurooncol.*, 78:7–14, 2006.

[12] M. Johannsen, U. Gneveckow, L. Eckelt, A. Feussner, N. Waldofner, R. Scholz, S. Deger, P. Wust, S.A. Loening, and A. Jordan. Clinical hyperthermia of prostate cancer using magnetic nanoparticles: Presentation of a new interstitial technique. *International Journal of Hyperthermia*, pages 1–11, 2005.

[13] K. M. Krishnan. Biomedical nanomagnetics: A spin through possibilities in imaging, diagnostics, and therapy. *IEEE Trans. Magn.*, 46:2523, 2010.

[14] Q. A. Pankhurst, N. K. T Thanh, S. K. Jones, and J. Dobson. Progress in applications of magnetic nanoparticles in biomedicine. *J. Phys. D: Appl. Phys.*, 42, 2009.

[15] B. D. Cullity and C. D.Graham. *Introduction to Magnetism and Magnetic Materials*. IEEE Press, Wiley, 2009.

[16] D. C. Jiles. *Introduction to Magnetism and Magnetic Materials*. Chapman and Hall, 1994.

[17] C. Tannous and J. Gieraltowski. The Stoner-Wohlfarth model of ferromagnetism. *Eur. J. Phys.*, 29: 475–487, 2008.

[18] B. Weise. *University of York*. Experimental data, 2012.

[19] K. O'Grady. PhD thesis, UNCW, Bangor, UK, 1982.

[20] L. Neel. Influence des flucuations thermiques a l'aimantation des particules ferromagnetiques. *C. R. Acad. Sci*, 228:664–8, 1949.

[21] E. Kneller. *Proceedings of the International Conference on Magnetism, Nottingham 1964*. Physical Society, London, 1965. page 174.

[22] C. P. Bean and J. D. Livington. Superparamagnetism. *J. Appl. Phys.*, 30:S120, 1959.

[23] R. Street and J. C. Woolley. A study of magnetic viscosity. *Proc. Phys. Soc. A*, 62:562, 1949.

[24] M. P. Sharrock. Time-dependent magnetic phenomena and particle size effects in recording media. *IEEE Trans. Magn.*, 26:193–197, 1990.

[25] R. W. Chantrell, G. N. Coverdale, and K. O'Grady. Time dependence and rate dependence of the coercivity of particulate recording media. *J. Phys. D: Appl. Phys.*, 21:1469, 1988.

[26] M. El-Hilo, A. M. de Witte, and K. O'Grady. The sweep rate dependence of coercivity in recording media. *J. Magn. Magn. Mater.*, 117:307–10, 1992.

[27] A. M. de Witte, M. El-Hilo, K. O'Grady, and R. W. Chantrell. sweep rate measurements of coercivity in particulate recording media. *J. Magn. Magn. Mater.*, 120:184–6, 1993.

[28] M. I. Shliomis. Magnetic fluids. *Sov. Phys. Usp.*, 17:153, 1974.

[29] R. Hergt, S. Dutz, R. Müller, and M. Zeisberger. Magnetic particle hyperthermia: nanoparticle magnetism and materials development for cancer therapy. *J. Phys. Condens. Matter*, 18:S2919–34, 2006.

[30] G. Glöckl, R. Hergt, M. Zeisberger, S. Dutz, S. Nagel, and W. Weitschies. The effect of field parameters, nanoparticle properties and immobilization on the specific heating power in magnetic particle hyperthermia. *J. Phys. Condens. Matter*, 18:S2935–49, 2006.

[31] R. Ramprasad, P. Zurcher, M. Petras, M. Miller, and P. Renaud. Magnetic properties of metallic ferromagnetic nanoparticle composites. *J. Appl. Phys.*, 96:519, 2004.

[32] Q. A. Pankhurst, J. Connolly, S. K. Jones, and J. Dobson. Applications of magnetic nanoparticles in biomedicine. *J. Phys. D: Appl. Phys.*, 36:R167–81, 2003.

[33] P. C. Fanin, B. K. P. Scafea, and S. W. Charlesb. Relaxation and resonance in ferrofluids. *J. Magn. Magn. Mater.*, 122:159–63, 1993.

[34] L. Neel. *C. R. Acad. Sci*, 224:1550, 1947.

[35] R. W. Chantrell, G. N. Coverdale, M. El-Hilo, and K. O'Grady. Modelling of interaction effects in fine particle systems. *J. Magn. Magn. Mater.*, 157/8:250–255, 1996.

[36] F. Burrows, C. Parker, R. F. L. Evans, Y. Hancock, O. Horkova, and R. W. Chantrell. Energy losses in interacting fine-particle magnetic composites. *J. Phys. D: Appl. Phys.*, 43:474010, 2010.

[37] I. Koh and L. Josephson. Magnetic nanoparticles sensors. *Sensors*, 9:8130–8145, 2009.

[38] M. Ma, Y. Wu, J. Zhou, Y. Sun, Y. Zhang, and N. Gu. Size dependence of specific power absorption of Fe_3O_4 particles in AC magnetic field. *J. Magn. Magn. Mater.*, 268:33–39, 2004.

[39] R. Hergt, S. Dutz, and M. Röder. Effects of size distribution on hysteresis losses of magnetic nanoparticles for hyperthermia. *J. Phys. Condens. Matter*, 18:385214, 2008.

[40] R. Müller, R. Hergt, S. Dutz, M. Zeisberger, and W. Gawalek. Nanocrystalline iron oxide and Ba ferrite particles in the superparamagnetismferromagnetism transition range with ferrofluid applications. *J. Phys. Condens. Matter*, 18:S2527–42, 2006.

[41] M. Kallumadil, M. Tada, T. Nakagawa, M. Abe, P. Southern, and Q. A. Pankhurst. Suitability of commercial colloids for magnetic hyperthermia. *J. Magn. Magn. Mater.*, 321:1509–13, 2009.

[42] K. O'Grady. Private Communication.

[43] R. E. Rosensweig. Heating magnetic fluid with alternating magnetic field. *J. Magn. Magn. Mater.*, 252:370–4, 2002.

[44] Y. S. Chen, Y. C. Hung, I. Liau, and G. S. Huang. Assessment of the in vivo toxicity of gold nanoparticles. *Nanoscale Res. Lett.*, 4:858–64, 2009.

[45] T. L. Kline, Y. H. Xu, Y. Jing, and J. P. Wang. Biocompatible high-moment FeCo-Au magnetic nanoparticles for magnetic hyperthermia treatment optimization. *J. Magn. Magn. Mater.*, 321:1525–1528, 2009.

[46] B. Bittova1, J. Poltierova-Vejpravova, A. G. Roca, M. P. Morales, and V. Tyrpekl. Effects of coating on magnetic properties in iron oxide nanoparticles. *J. Phys.: Conf. Ser.*, 200:072012, 2010.

[47] C. L. De Castro and B. S. Mitchell. Chapter 1: Nanoparticles from Mechanical Attrition. In M-I. Baraton, editor, *Synthesis, functionalization and surface treatment of nanoparticles*. American Scientific Publishers, 2003.

[48] A. G. Roca, R. Costo, A. F. Rebolledo, S. Veintemillas-Verdaguer, P. Tartaj, T. González-Carreño, M. P. Morales, and C. J. Serna. Progress in the preparation of magnetic nanoparticles for applications in biomedicine. *J. Phys. D: Appl. Phys.*, 42:224002, 2009.

[49] T. Hyeon, S. S. Lee, J. Park, Y. Chung, and H. B. Na. Synthesis of highly crystalline and monodisperse maghemite nanocrystallites without a size-selection process. *J. Am. Chem. Soc.*, 123:12798–801, 2001.

[50] http://www.nanotherics.com/products/magnetherm.

[51] A. C. Silva, T. R. Oliveira, J. B. Mamani, S. M. F. Malheiros, L. Malavolta, L. F. Pavon, T. T. Sibov, E. Amaro Jr., A. Tannús, E. L. G. Vidoto, M. J. Matins, R. S. Santos, and L. F. Gamarra. Application of hyperthermia induced by superparamagnetic iron oxide nanoparticles in glioma treatment. *Int. J. Nanomedicine*, 6:591–603, 2011.

[52] R. F. Barth. Rat brain tumor models in experimental neuro-oncology: The 9L, C6, T9, F98, RG2 (D74), RT-2 and CNS-1 Gliomas. *Int. J. Neurooncol.*, 36:91–102, 1998.

[53] S. M. Cassim, A. J. Giustini, A. A. Petryk, R. A. Strawbridge, and P. J. Hoopes. Iron oxide nanoparticle hyperthermia and radiation cancer treatment. *Proc. of SPIE*, 7181, 2009.

[54] http://www.multifun-project.eu.

[55] R. W. Chantrell, N. Walmsley, J. Gore, and M. Maylin. Calculations of the susceptibility of interacting superparamagnetic particles. *Phys. Rev. B*, 63:024410, 2000.

[56] M. Matsumoto and T. Nishimura. Mersenne twister: a 623-dimensionally equidistributed uniform pseudo-random number generator. *ACM T. Model. Comput. S.*, 8:3–30, 1998.

[57] M. El-Hilo, K. O'Grady, P. I. Mayo, R. W.Chantrell, I. L. Sanders, and J. K. Howard. The effects of different demagnetisation processes on interaction effects in thin film media. *IEEE Trans. Magn.*, 28: 3283, 1992.

[58] N. Metropolis, A. W. Rosenbluth, M. N. Rosenbluth, A. H. Teller, and E. Teller. Equation of state calculations by fast computing machines. *J. Chem. Phys.*, 21:1087, 1953.

[59] H. Pfeiffer. Determination of anisotropy field distribution in particle assemblies taking into account thermal fluctuations. *Phys. Status Solidi a*, 118, 1990.

[60] T. Ibusuki, S. Kojima, O Kitakami, and Y. Shimada. Magnetic anisotropy and behaviors of Fe nanoparticles. *ieeetom*, 37:2223, 2001.

[61] P. Guardia, B. Batlle-Brugal, A. G. Roca, O. Iglesias, M. P. Morales, C. J. Serna, A. Labarta, and X. Batlle. Surfactant effects in magnetite nanoparticles of controlled size. *J. Magn. Magn. Mater.*, 316:e756–9, 2007.